

An Analog Comparison between Rapidly and Slowly Intensifying Tropical Cyclones

JANNETTA C. RICHARDSON,^a RYAN D. TORN,^a AND BRIAN H. TANG^a

^a *Department of Atmospheric and Environmental Sciences, University at Albany, State University of New York, Albany, New York*

(Manuscript received 29 September 2021, in final form 12 May 2022)

ABSTRACT: To better understand the conditions that favor tropical cyclone (TC) rapid intensification (RI), this study assesses environmental and storm-scale characteristics that differentiate TCs that undergo RI from TCs that undergo slow intensification (SI). This comparison is performed between analog TC pairs that have similar initial intensity, vertical wind shear, and maximum potential intensity. Differences in the characteristics of RI and SI TCs in the North Atlantic and western North Pacific basins are evaluated by compositing and comparing data from the fifth-generation European Centre for Medium-Range Weather Forecasts (ECMWF) Re-Analysis (ERA5) and the Gridded Satellite (GridSat) dataset. In the period leading up to the start of RI, RI TCs tend to have a stronger and deeper vortex that is more vertically aligned than SI TCs. Additionally, surface latent heat fluxes are significantly larger in RI TCs prior to the intensity change period, compared to SI TCs. The largest surface latent heat flux differences are initially located to the left of shear; subsequently, upshear and right-of-shear differences amplify, resulting in a more symmetric distribution of surface latent heat fluxes in RI TCs. Increasing azimuthal symmetry of surface latent heat fluxes in RI TCs, together with an increasing azimuthal symmetry of horizontal moisture flux convergence, promote the upshear migration of convection in RI TCs. These differences, and their evolution before and during the intensity change period, are hypothesized to support the persistence and invigoration of upshear convection and, thus, a more symmetric latent heating pattern that favors RI.

KEYWORDS: Atmosphere; North Atlantic Ocean; North Pacific Ocean; Tropical cyclones; Reanalysis data

1. Introduction

Tropical cyclone (TC) intensity change is dependent on complex physical processes interacting across a broad spectrum of spatial and temporal scales. Skillful prediction of TC intensity change, especially rapid intensification (RI), remains limited (e.g., Kaplan et al. 2010; DeMaria et al. 2014; Fischer et al. 2019), in part because the multiscale interactions involved are not well understood. Consequently, RI, which is defined in the North Atlantic as a TC intensity increase of 30 kt (15.4 m s^{-1} ; $1 \text{ kt} \approx 0.51 \text{ m s}^{-1}$) or more in 24 h (Kaplan and DeMaria 2003), continues to be a major focus of research. Several environmental characteristics have been identified as being favorable for RI, including low vertical wind shear, high ocean heat content and tropospheric humidity (e.g., Kaplan and DeMaria 2003; Wang and Wu 2004; Hendricks et al. 2010; Rozoff and Kossin 2011; Kaplan et al. 2015; Rozoff et al. 2015). However, important aspects of TC RI remain uncertain, including the TC evolution leading up to RI and relevant factors in the TC environment and inner core that favor RI versus slow intensification (SI).

A few studies have compared the environmental characteristics of RI and SI TCs, with varying outcomes. Hendricks et al. (2010) found that the environments of RI TCs are comparable to that of SI TCs for North Atlantic and western North Pacific TCs over a 6-yr period (2003–08). A notable exception is that vertical wind shear is statistically significantly weaker in RI TCs than in SI TCs in the North Atlantic. Overall, Hendricks et al. (2010) argued that internal dynamics exert more important controls on RI than environmental

factors. Wang and Jiang (2021) conducted a longer climatological analysis of North Atlantic and eastern North Pacific TC environments using the Statistical Hurricane Intensity Prediction Scheme (SHIPS; DeMaria et al. 2005) developmental database. Their results, in contrast, indicated significant differences in environmental characteristics between RI and SI TCs. Using event-based definitions of RI and SI, they found that RI events in the North Atlantic and eastern North Pacific had weaker vertical wind shear, larger 200-hPa divergence, larger low-level and midlevel relative humidity, and were farther away from their maximum potential intensities compared to SI events. Given that SHIPS environmental parameters are mostly area averages of various atmospheric quantities that measure the TC environment, investigating asymmetries of these and other parameters could provide additional insight into factors that differentiate RI and SI.

As the aforementioned climatological studies indicated, vertical wind shear is a key factor influencing whether or not TCs undergo RI. Indeed, vertical wind shear is employed as a top-weighted predictor in the SHIPS rapid intensification index (SHIPS-RII; Kaplan et al. 2015) owing to the strong inverse relationship between the probability of RI and vertical wind shear magnitude (Kaplan and DeMaria 2003; Kaplan et al. 2010; Hendricks et al. 2010; Kaplan et al. 2015; Wang and Jiang 2021). Vertical wind shear tilts the TC vortex in the vertical and produces a wavenumber-1 asymmetry in convection, with convection enhanced downshear and suppressed upshear (Corbosiero and Molinari 2002, 2003; Chen et al. 2006; Hense and Houze 2012; Reasor et al. 2013). Shear also inhibits TC intensification through various mechanisms, such as ventilation of the upper-level warm core (Gray 1968; Frank and Ritchie 2001), ventilation of the core by midlevel dry air (Riehl and Malkus 1961; Emanuel et al. 2004; Tang and

Corresponding author: Jannetta Richardson, jrichardson@albany.edu

Emanuel 2010; Alland et al. 2021b), and downdraft ventilation that brings cooler and drier midlevel air toward the surface, and consequently, reduces the θ_e of the low-level inflow into the inner core (e.g., Riemer et al. 2010a,b, 2013; Alland et al. 2021a). Given the substantial influence of vertical wind shear on the TC structure and intensity, it is worth investigating how other factors could modulate the TC's response to shear to hinder or promote RI.

Despite the overwhelmingly negative impacts of vertical wind shear on TC intensity, RI can proceed in moderate to high shear, as evidenced in observations (e.g., Zawislak et al. 2016; Ryglicki et al. 2018a) and simulations (e.g., Zhang and Tao 2013; Judt and Chen 2016; Rios-Berrios et al. 2018; Ryglicki et al. 2018b). Improved understanding of how environmental and internal factors modulate the TC's response to moderate shear is especially needed, since intensity changes in moderate shear exhibit large variability and low predictability (e.g., Bhatia and Nolan 2013; Zhang and Tao 2013; Tao and Zhang 2015; Finocchio and Majumdar 2017). The RI of moderately sheared TCs can be considered in terms of the energetics and efficiency of the symmetric intensification process. A greater azimuthal extent of convection allows for greater projection of latent heating onto the symmetric mode, which is more favorable for intensification when the convection occurs at and within the radius of maximum wind (Nolan and Grasso 2003; Nolan et al. 2007; Pendergrass and Willoughby 2009; Vigh and Schubert 2009; Rogers et al. 2013). As such, factors that promote precipitation symmetrization are important to the intensification of sheared TCs (e.g., Rappin and Nolan 2012; Tao and Zhang 2014; Finocchio et al. 2016; Onderlinde and Nolan 2016; Zawislak et al. 2016; Munsell et al. 2017; Nguyen et al. 2017; Shimada et al. 2017; Rios-Berrios et al. 2018), and may be relevant for favoring RI versus SI.

Other factors such as midlevel relative humidity, low-level θ_e and sea surface temperature (SST) can affect precipitation symmetry and intensification rates. In a case study of Hurricane Edouard (2014), Zawislak et al. (2016) found that intensification was facilitated by the removal of the relatively dry midtropospheric layers via an increase in upshear precipitation. Furthermore, high SSTs allowed for the recovery of low- θ_e boundary layer air via surface fluxes, increasing the convective available potential energy downshear and allowing deep convection to persist upshear (Rogers et al. 2016). In a composite study of moderately sheared TCs, Nguyen et al. (2019) found a similar relationship between enhanced upshear surface fluxes in RI TCs and boundary layer recovery of downdraft-cooled inflow. They proposed that the resulting enhancement of downshear lower-tropospheric instability allowed for upshear propagation of convection.

The relative importance of axisymmetric versus asymmetric mechanisms to TC intensification and RI remains a topic of debate. Some studies have shown that RI of sheared TCs can be triggered by highly asymmetric convective bursts (CBs) in the inner-core region (e.g., Molinari and Vollaro 2010; Nguyen and Molinari 2012; Chen and Gopalakrishnan 2015). However, multiple satellite-based studies have demonstrated that RI is most often associated with an increased azimuthal and areal coverage of precipitation and convection (e.g.,

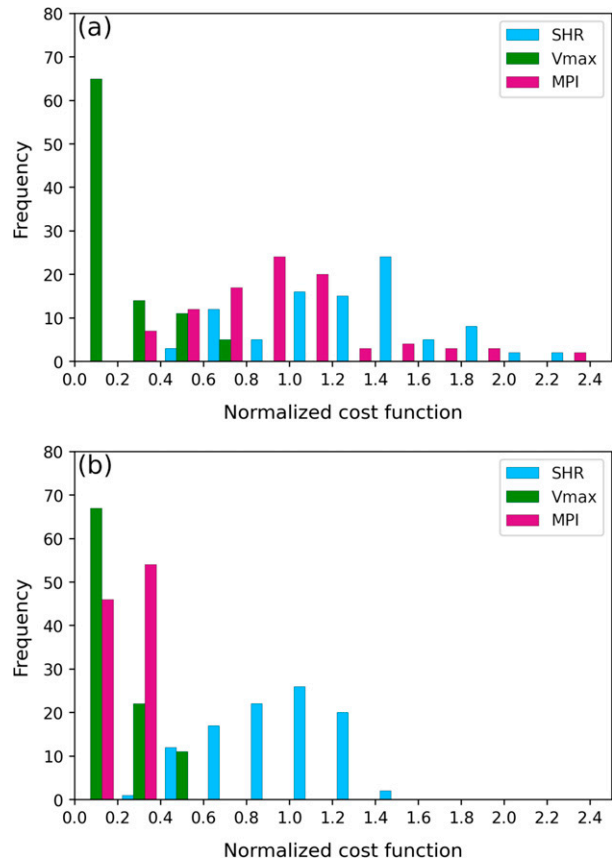


FIG. 1. Normalized difference contributions of vertical wind shear (blue), initial intensity (green), and maximum potential intensity (purple) to the analog cost functions in the (a) North Atlantic and (b) western North Pacific.

Zagrodnik and Jiang 2014; Tao and Jiang 2015; Alvey et al. 2015; Tao et al. 2017; Fischer et al. 2018). Kieper and Jiang (2012) discovered that a distinct, symmetric cyan ring in 37-GHz microwave images, which is indicative of symmetric, shallow to moderate liquid clouds and rain, appears as a precursor to RI. The convective characteristics of RI versus SI can be further clarified by comparing the evolution of convection of RI and SI TCs, while controlling for the effects of vertical wind shear and other parameters that influence RI.

The main objective of this study is to better understand the environmental and storm-scale factors that affect TC RI versus SI. Although numerous studies have compared RI and non-RI TCs, few studies have compared RI and SI TCs. Furthermore, prior studies compared RI and non-RI factors across a broad range of initial intensities, maximum potential intensities (MPIs), and vertical wind shear magnitudes. Given that these three factors exhibit significant controls on RI (e.g., Kaplan and DeMaria 2003; Kaplan et al. 2010), and thus, can potentially mask the influence of other factors, it will be useful to control for these factors. Moreover, we seek to understand the temporal and spatial evolutions of environmental and storm-scale characteristics in a shear-relative framework because of the distinct organization of the TC structure by

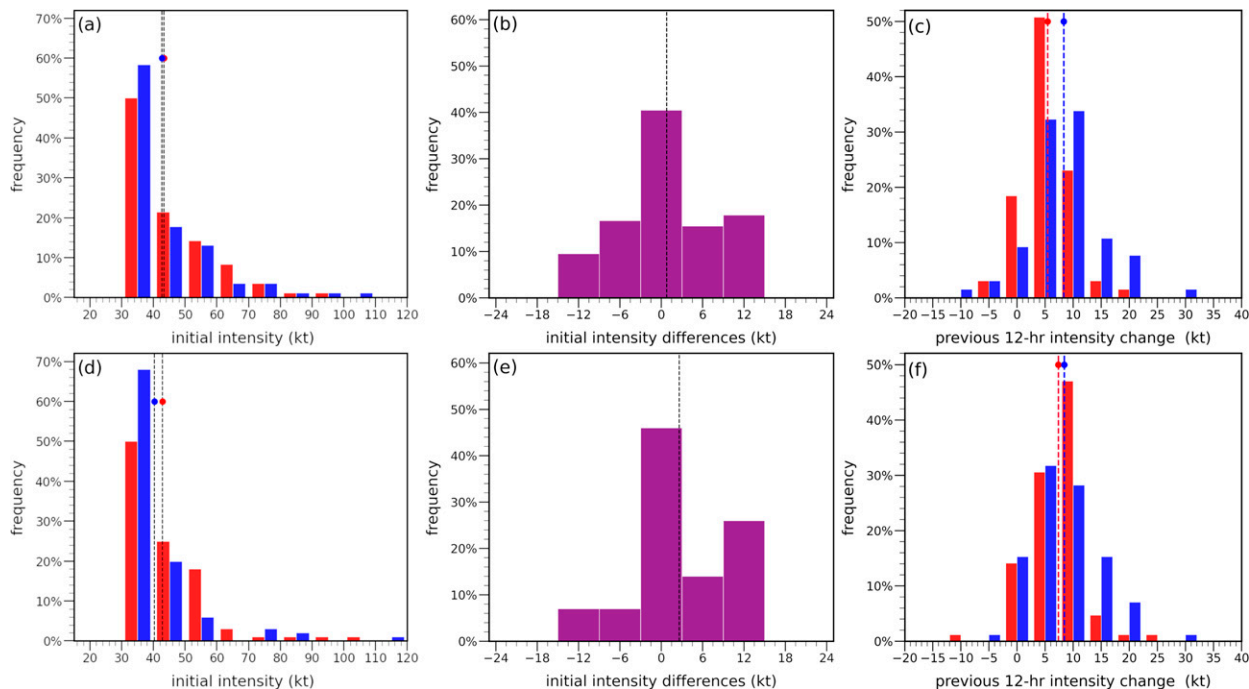


FIG. 2. Distributions of (a),(d) initial intensity (kt) of analog RI (red) and SI (blue) TCs; (b),(e) initial intensity difference (kt) between analogs; and (c),(f) previous 12-h intensity change of analog TCs in (top) the North Atlantic and (bottom) the western North Pacific. The mean of each distribution is represented by a dashed line, and the colored circles denote the mean of the RI (red) and SI (blue) groups.

vertical wind shear. Also, less is known about the temporal and spatial evolutions of these characteristics leading up to the start of RI.

The current study addresses the above considerations by employing an analog method that compares TCs that undergo RI with a set of analog TCs that have similar initial intensity, vertical wind shear, and MPI, but undergo SI. To the best of the authors' knowledge, this is the first study that has sought to compare RI and SI TCs while directly considering similar shear and MPI environments along with initial intensities. Additionally, by examining analog TCs in the North Atlantic and western North Pacific basins, this work also analyzes interbasin similarities in the evolution of the environmental and storm-scale characteristics.

The remainder of this paper is arranged as follows. Section 2 describes the analog selection method and the datasets. Section 3 describes the results of the composite analysis of the environmental and storm-scale characteristics. Last, section 4 provides a summary of key findings.

2. Data and methods

a. Datasets

This study investigates TCs that developed in the North Atlantic basin during 1982–2019 and in the western North Pacific basin during 1990–2017. TC observations are obtained from the International Best Track Archive for Climate Stewardship (IBTrACS) dataset (Knapp et al. 2010). The 6-hourly

TC center position, distance to the nearest landmass, and maximum sustained 10-m wind speed best track data issued by the National Hurricane Center (NHC) are retrieved for North Atlantic TCs, and corresponding best track data issued by the Joint Typhoon Warning Center (JTWC) are retrieved for western North Pacific TCs. The best track data are filtered so that all records of tropical waves, tropical depressions, subtropical and extratropical cyclones are removed. Additionally, any records within 100 km of land are removed to eliminate potential land interactions. For the remaining records, 24-h intensity change was calculated.

Atmospheric fields are obtained from the fifth-generation European Centre for Medium-Range Weather Forecasts (ECMWF) Re-Analysis (ERA5; Hersbach et al. 2020). ERA5 provides global data with a $0.28^\circ \times 0.28^\circ$ horizontal grid spacing on 137 atmospheric levels up to a pressure of 0.01 hPa at 1-hourly temporal resolution. The TC location in ERA5 is determined by searching for the grid point that represents the minimum sea level pressure centroid within a $\sim 3^\circ$ square box centered on the best track center location. This approach allows for instances in which reasonable deviations exist between the ERA5 and best track TC center locations. TC cases are rejected if the ERA5 center location consistently falls outside the $\sim 3^\circ$ square box during the period of interest. There are important caveats to the use of reanalyses to investigate TCs and their environments. A combination of factors, including the scarcity of in situ observations, the relatively low spatial and temporal resolution, and the dependence on the parameterization of subgrid scale processes, contribute to

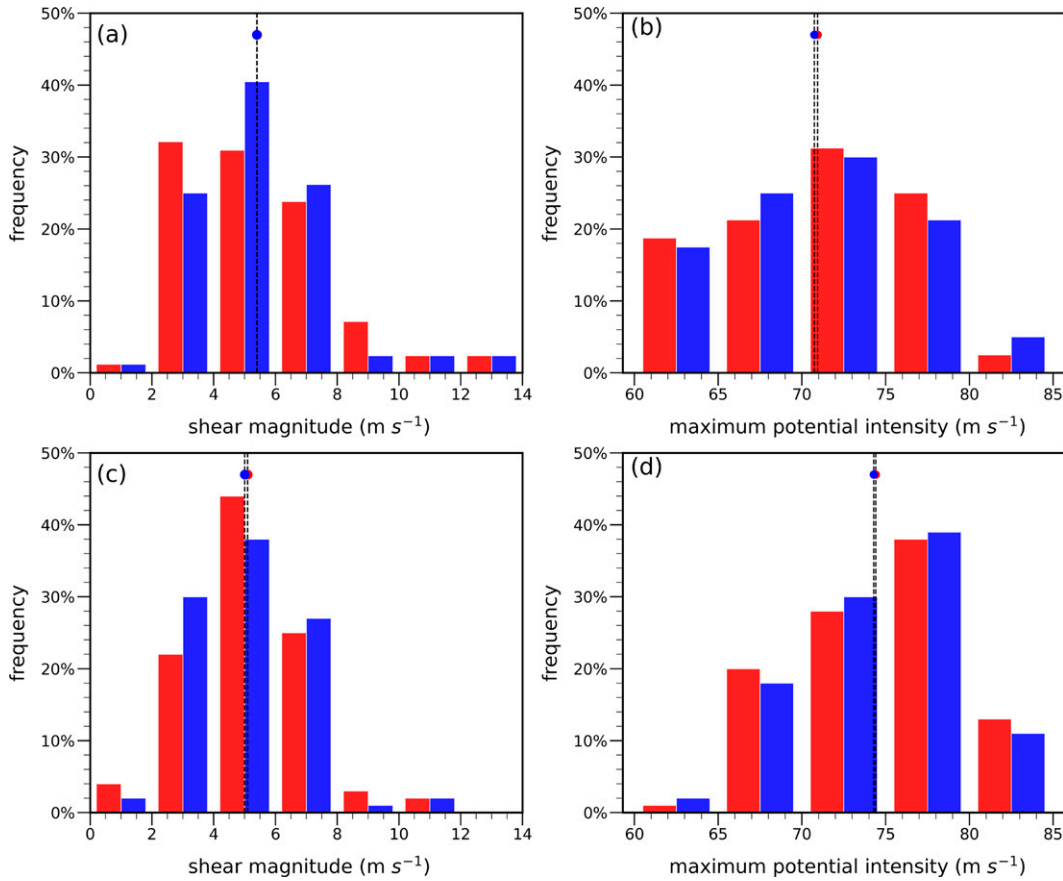


FIG. 3. Distributions of (a),(c) vertical wind shear magnitudes ($m s^{-1}$) and (b),(d) MPI ($m s^{-1}$) of analog RI (red) and SI (blue) TCs in the (top) North Atlantic and (bottom) western North Pacific. The mean of each distribution is represented by a dashed line along with a colored circle.

misrepresentations of TC position, intensity and structural evolution by reanalyses (Schenkel and Hart 2012; Hodges et al. 2017). Despite such limitations, the ERA5 offers improved data quality and degree of detail compared to previous products. For example, Dullaart et al. (2020) compared TC representations from the ERA5 to those from the ERA-Interim (Dee et al. 2011) and found that the ERA5’s improved data assimilation scheme and enhanced spatial and temporal resolutions resulted

in a 58% reduction in the root mean squared errors of TC wind speeds within 200 km of the center. Overall, ERA5 allows for a more realistic representation of TCs and their near environments and presents an improved option for investigating the evolution of broadscale aspects of TCs and their environments.

To analyze TC convective characteristics, infrared (IR) brightness temperature data are retrieved from the GridSat-B1 dataset (Knapp et al. 2011). GridSat-B1 IR brightness temperature

TABLE 1. Mean values of intensity (kt), shear magnitude ($m s^{-1}$), and MPI ($m s^{-1}$) at 6-hourly intervals for North Atlantic analog TCs.

| Hour | RI | | | SI | | |
|-------|-----------|----------------------|--------------------|-----------|----------------------|--------------------|
| | Vmax (kt) | Shear ($m s^{-1}$) | MPI ($m s^{-1}$) | Vmax (kt) | Shear ($m s^{-1}$) | MPI ($m s^{-1}$) |
| -12 h | 39.9 | 5.5 | 70.0 | 35.8 | 5.3 | 70.8 |
| -6 h | 40.3 | 5.1 | 70.3 | 37.8 | 5.4 | 70.9 |
| 0 h | 43.4 | 5.3 | 70.7 | 42.6 | 5.4 | 70.7 |
| 6 h | 49.5 | 5.4 | 70.4 | 46.3 | 5.4 | 70.3 |
| 12 h | 56.1 | 5.2 | 70.1 | 49.9 | 5.1 | 70.2 |
| 24 h | 75.8 | 5.7 | 70.1 | 55.0 | 5.9 | 70.0 |

TABLE 2. Mean values of intensity (kt), shear magnitude ($m s^{-1}$), and MPI ($m s^{-1}$) at 6-hourly intervals for western North Pacific analog TCs.

| Hour | RI | | | SI | | |
|-------|-----------|----------------------|--------------------|-----------|----------------------|--------------------|
| | Vmax (kt) | Shear ($m s^{-1}$) | MPI ($m s^{-1}$) | Vmax (kt) | Shear ($m s^{-1}$) | MPI ($m s^{-1}$) |
| -12 h | 36.8 | 5.3 | 75.9 | 32.7 | 5.6 | 75.7 |
| -6 h | 39.4 | 5.3 | 75.8 | 35.3 | 4.8 | 75.2 |
| 0 h | 42.9 | 5.1 | 75.5 | 40.3 | 5.0 | 75.1 |
| 6 h | 49.2 | 5.0 | 75.1 | 43.5 | 5.0 | 74.9 |
| 12 h | 56.6 | 5.1 | 74.7 | 46.7 | 4.9 | 74.5 |
| 24 h | 76.8 | 5.2 | 73.8 | 53.7 | 5.3 | 74.0 |

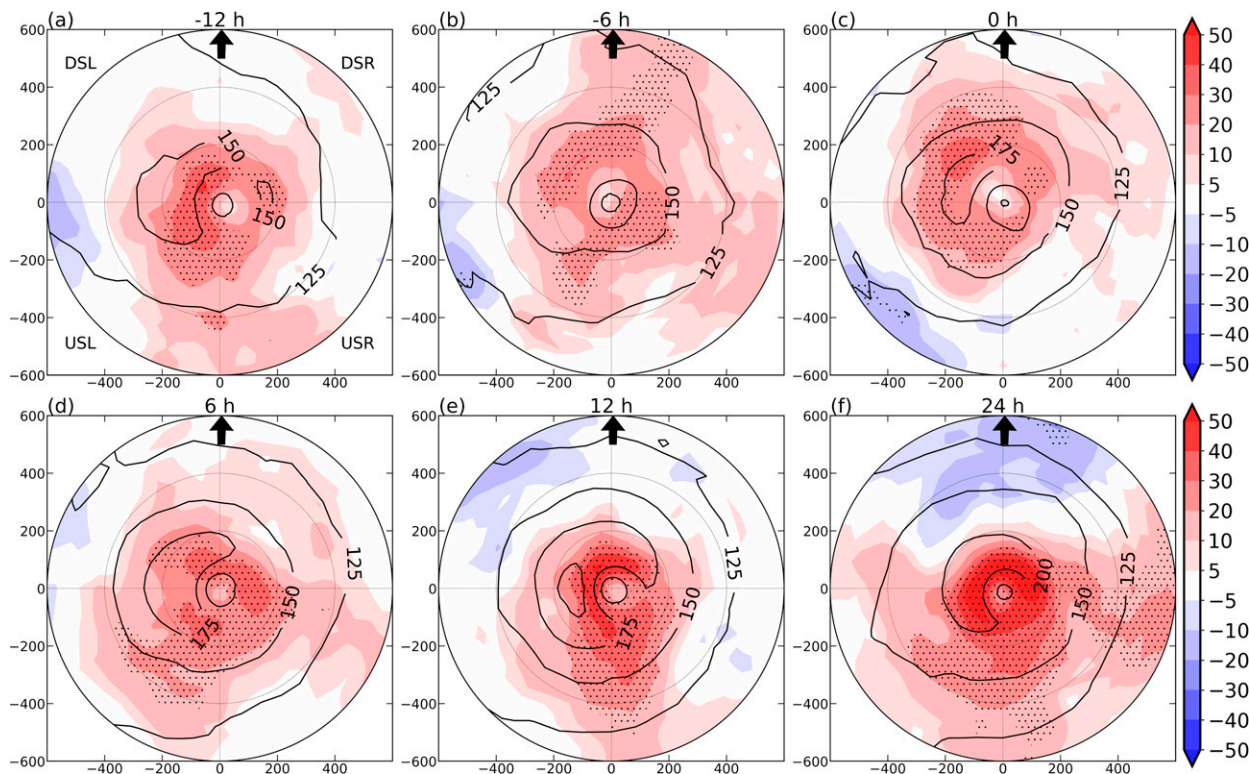


FIG. 4. Evolution of composite differences of surface latent heat flux (W m^{-2}) between analog RI and SI TCs (shaded; RI minus SI) and mean of the combined RI and SI TC samples (contoured) in the North Atlantic. Panels show 6-hourly time stamps relative to the onset of RI and SI (0 h), where negative time stamps indicate before RI and SI onset and positive time stamps indicate after onset. Stippling indicates statistically significant differences at the 95% confidence interval. The arrow denotes the shear vector direction. Shear-relative quadrants are labeled: downshear-right (DSR), downshear-left (DSL), upshear-left (USL), and upshear-right (USR). Range rings (gray circles) are every 200 km.

data are available at a 3-hourly temporal resolution and $0.07^\circ \times 0.07^\circ$ horizontal resolution, which allows for consistent sampling of the TC convection and for an observational element to complement the analysis done with the ERA5.

b. Intensity change categories

Two intensity change groups are defined for comparison: rapidly intensifying (RI) and slowly intensifying (SI) TCs. Following Kaplan and DeMaria (2003), RI is defined as an increase in the maximum sustained wind speed of 30 kt or more in 24 h. For simplicity, this 30-kt threshold is applied across all basins. SI cases are defined as 24-h intensity changes between 10 and 15 kt. The 15-kt upper bound, versus using 25 or 30 kt, allows for greater differentiation of factors that contribute to RI versus SI and accounts for the uncertainty in the best track intensity (Torn and Snyder 2012; Landsea and Franklin 2013). We tested the sensitivity of our results to the choice of 15- and 20-kt SI upper bounds. Both choices yielded similar results, but the 15-kt upper bound does yield a stronger signal.

This paper focuses on differences in the evolution of environmental and storm-scale characteristics associated with the first 24-h period of RI and SI that occurred in TCs. Doing so allows for a more straightforward comparison of TCs both

leading up to and during the intensification period. For example, a TC can satisfy RI criteria for multiple overlapping 24-h periods (Kieper and Jiang 2012), and factors that are important for the onset of RI (versus SI) may differ from factors that are important for the continuation of RI. Our focus is mainly on the former. Additionally, since the first instance of RI and SI tended to occur early in a TC's lifetime, this approach mitigates against large differences in TC age between analog pairs, the selection of which is described next.

c. Analog selection and compositing method

The objective of the analog selection procedure is to find, for each RI case, a comparable SI case based on a small subset of environmental and TC characteristics that are important to TC intensity change: maximum potential intensity (MPI), vertical wind shear, and initial TC intensity. By using TC analogs to control for these three parameters, similar to the analog method of Rios-Berrios and Torn (2017), other potentially relevant environmental and storm-scale factors that differentiate RI from SI may be assessed. Vertical wind shear and MPI data are extracted from the SHIPS (Kaplan and DeMaria 1995) dataset. The initial step in the analog algorithm involves comparing the value of the analog parameters

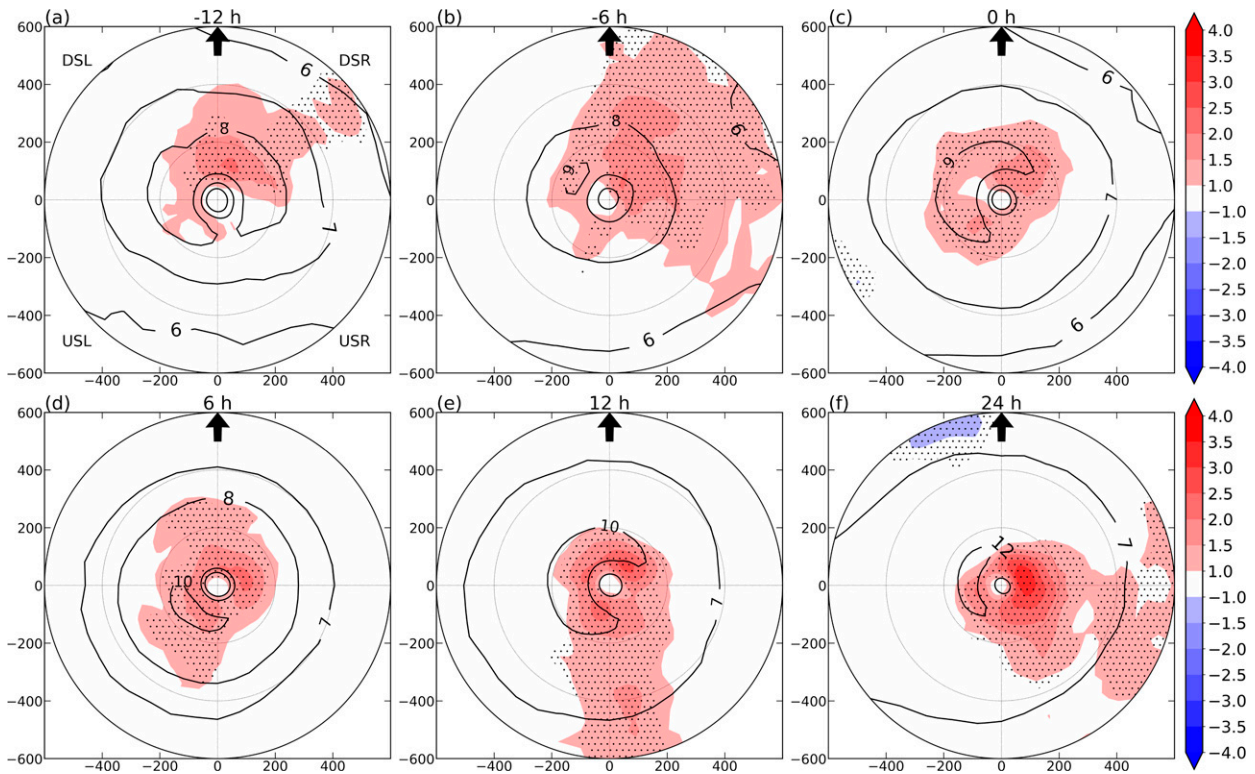


FIG. 5. As in Fig. 4, but for 10-m wind speeds (m s^{-1}).

of a particular RI case at each 6-hourly interval during the 24-h intensity change period (i.e., $t = 0, 6, 12, 18,$ and 24 h) to that of all other SI cases within that basin. Note that $t = 0$ h is defined as the start of the 24-h period for which the RI (SI) criterion is satisfied, as diagnosed using best track data. The analog comparison is achieved by computing a cost function J , similar to that of Halperin and Torn (2018). For a particular RI case, this cost function is computed for every possible SI case pairing in the basin as follows:

$$J = \left| \frac{V_{\max_{\text{RI}}} - V_{\max_{\text{SI}}}}{\sigma_{V_{\max}}} \right|_{t=0} + \sum_{t=0}^{24} \left| \frac{\text{SHR}_{\text{RI}} - \text{SHR}_{\text{SI}}}{\sigma_{\text{SHR}}} \right| + \sum_{t=0}^{24} \left| \frac{\text{MPI}_{\text{RI}} - \text{MPI}_{\text{SI}}}{\sigma_{\text{MPI}}} \right|, \quad (1)$$

where SHR is the magnitude of the vertical wind shear, MPI is the MPI, V_{\max} is the best track maximum wind speed, and σ is the standard deviation of the variable for all eligible TCs. The cost function quantifies the degree of similarity between an RI and SI case by summing the normalized differences in the intensity at $t = 0$ h [first term on rhs of Eq. (1)], the normalized differences in vertical wind shear at $t = 0, 6, 12, 18,$ and 24 h [second term on rhs of Eq. (1)], and the normalized differences in MPI at $t = 0, 6, 12, 18,$ and 24 h [third term on rhs of Eq. (1)]. All SI cases are then ranked in order of suitability as an analog for an RI case based on the magnitude of their respective J values. The specific SI case that results

in the minimum value of J is tentatively selected as the analog of the RI case. This procedure is repeated for each RI case.

In situations where one SI case is chosen as the best analog for multiple RI cases, the algorithm assigns the SI case to the RI case that has the largest minimized J (i.e., the “hardest” to match). Then, the algorithm determines the next best available SI analog for each of the remaining RI cases. A limitation of the analog method can be difficulty in finding “good analogs” within the study period. In the final step of the algorithm, an analog pair is rejected if a component of the cost function [any term in Eq. (1)] exceeds 1.5 standard deviations from that component’s mean value for the sample of analog pairs. The choice of 1.5 standard deviations serves as a good balance to enforce quality control of the analog pairs and to have an adequate sample size. This procedure results in 88 analog TC pairs in the North Atlantic basin during 1982–2019 and 100 analog TC pairs in the western North Pacific basin during 1990–2017. Figure 1 shows the distribution of the three components of J for the final set of analog TCs in each basin. The distributions indicate that, on average, vertical wind shear differences make the largest contribution to the total cost function in both basins, particularly the western North Pacific. This pattern suggests that it is more difficult to find RI and SI TCs that have similar 24-h vertical wind shear evolutions compared to the initial intensity and 24-h MPI evolutions, likely due to the more variable nature of vertical wind shear. The analog selection procedure generally results in similar distributions of

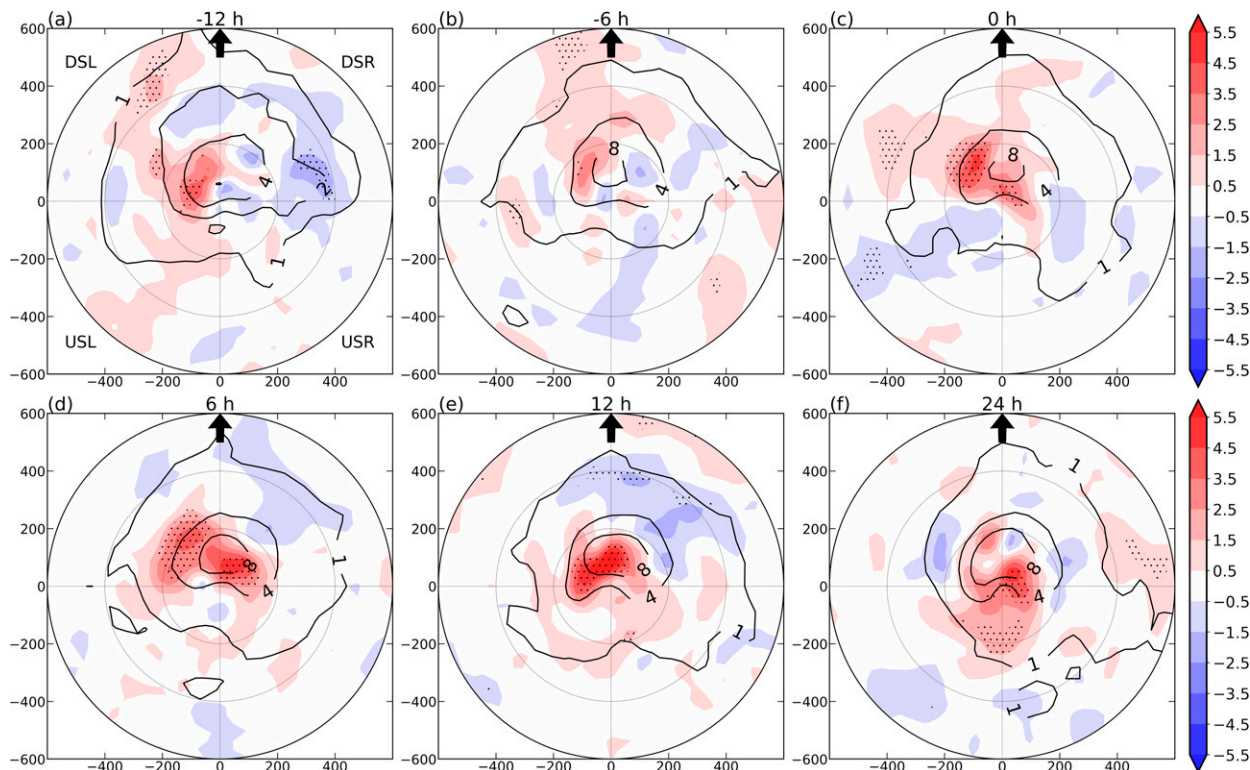


FIG. 6. As in Fig. 4, but for vertically integrated horizontal moisture flux convergence ($10^{-4} \text{ kg m}^{-2} \text{ s}^{-1}$).

initial intensity (Fig. 2), and 0–24-h averaged vertical wind shear and MPI (Fig. 3) for the RI and SI groups. Tables 1 and 2 illustrate the mean values of analog parameters at 6-hourly intervals from -12 to 24 h. Throughout the 0–24-h intensification period, the mean shear magnitudes and MPI values of RI and SI TC analogs remain within 1 m s^{-1} in both the North Atlantic and western North Pacific basins.

After the analog pairs are selected, ERA5 and brightness temperature fields associated with the TCs are constructed in a storm-centered, shear-relative framework. Fields are rotated with respect to the SHIPS vertical wind shear direction, such that the shear vector points northward. Differences between analog TC fields are computed (RI minus SI) and composited. A bootstrap resampling technique, similar to Rios-Berrios et al. (2016), is used to test the statistical significance of the composite differences between RI and SI analogs at the 95% confidence level. The null hypothesis, used to test the statistical significance at each grid point, is that the composite difference between the RI cases and their SI analogs is statistically the same as the composite difference between two groups that are randomly sampled from the combined RI and SI dataset. The initial step in this procedure is to randomly sample two equal-sized groups from the combined RI and SI dataset. The size of the random groups is the same as that of the number of analog pairs (e.g., 88 in the North Atlantic). Next, the composite difference is computed between the two randomly sampled groups. This random sampling is repeated a total of 1000 times, and the resulting

composite differences collectively form a null distribution. Finally, the observed composite difference between the actual RI and SI cases is compared to the null distribution to determine whether the null hypothesis can be rejected at the 95% confidence level.

This study does not exclude an SI period and an RI period associated with the same TC from being counted in the respective RI and SI samples. This approach allows for the inclusion of instances in which SI precedes RI, such that a key question can be addressed: why did RI not occur earlier in that TC's lifetime? It should be noted that additional tests conducted on completely independent RI and SI samples, in which only one case is included in the analyses if both RI and SI occur in a single TC, revealed environmental and storm-scale difference patterns that were largely consistent with the results presented in this study.

3. Results

a. North Atlantic

1) SURFACE FLUXES

First, we compare surface flux patterns between analog RI and SI TCs. This analysis focuses on the latent heat flux component of the total surface enthalpy flux, since latent heat fluxes dominated over sensible heat fluxes in the TC environments, consistent with previous observational studies (e.g., Jaimes et al. 2015; Gao et al. 2016; Nguyen et al. 2019). Figure 4

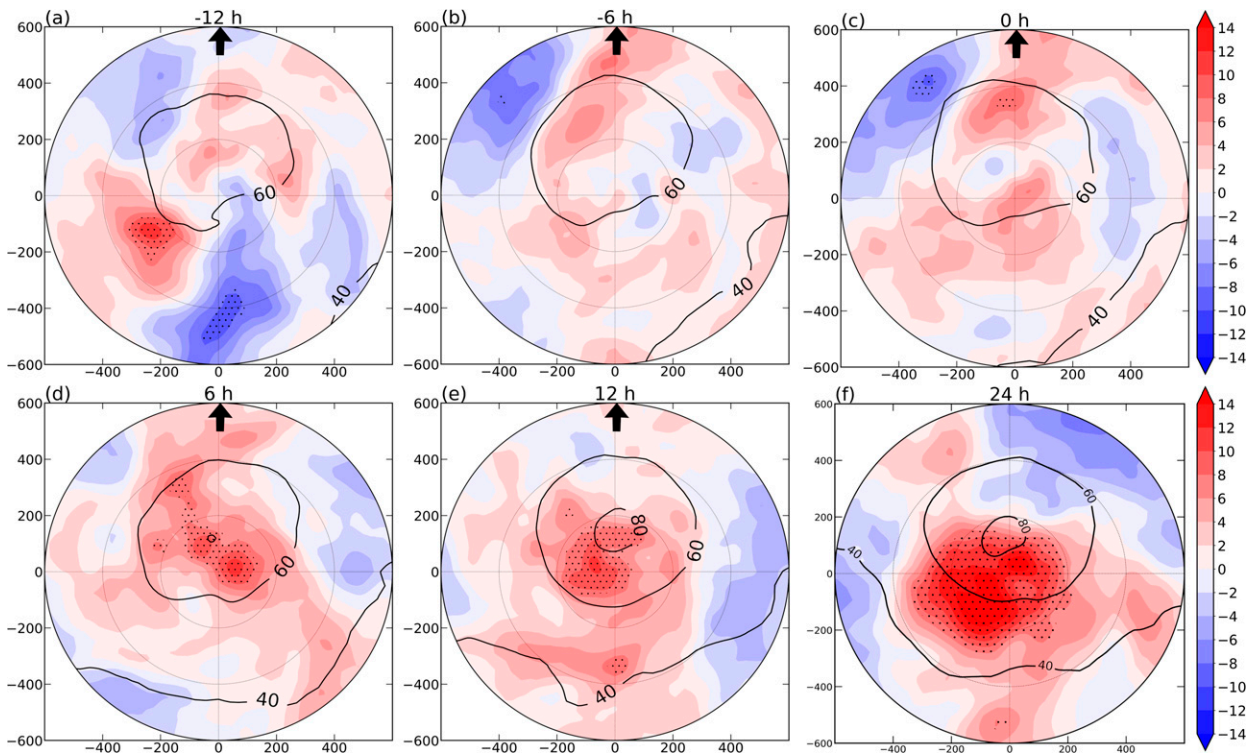


FIG. 7. As in Fig. 4, but for 400-hPa relative humidity (%).

shows the evolution from -12 to 24 h of the mean surface latent heat flux of the combined RI and SI sample (black contours) and composite differences (shading). Figure panels represent 6-hourly time intervals relative to 0 h, which is the start of the RI and SI periods, as diagnosed using best track data. The mean surface latent heat fluxes tend to be larger in the left-of-shear quadrants than right-of-shear quadrants. Composite differences between the two intensity change groups reveal that RI TCs generally have larger surface latent heat fluxes at all azimuths. Statistically significant positive differences are mostly present within 400 km of the TC center and are most pronounced in the inner-core region, within 200 km of the TC center.

At and before 0 h, the largest positive differences are generally confined to the left-of-shear quadrants, particularly downshear left, within the innermost 200 km, where surface latent heat fluxes are >30 W m^{-2} larger in RI TCs than SI TCs (Figs. 4a–c). After 0 h, positive differences amplify in all quadrants within the innermost 200 km. By the end of the intensity change period, surface latent heat fluxes in the inner-core region are over 60 W m^{-2} larger for RI TCs than SI TCs (Fig. 4f) owing to the difference in intensification rates, and the areal coverage of positive differences expands upshear. Thus, RI TCs are associated with larger magnitudes of surface latent heat fluxes leading up to RI onset and increasing azimuthal symmetry of surface latent heat fluxes during the 24-h intensity change period. These findings are qualitatively similar to those of modeling and observational studies that demonstrated linkages between enhanced surface latent heat fluxes

and faster intensification rates (e.g., Rappin and Nolan 2012; Onderlinde and Nolan 2016; Gao et al. 2016; Rios-Berrios and Torn 2017; Nguyen et al. 2019). Recent studies have shown that enhanced surface enthalpy fluxes in left-of-shear quadrants of RI TCs is a more favorable thermodynamic configuration for overcoming the effects of downdraft-induced low entropy air in left-of-shear and upshear quadrants (e.g., Wadler et al. 2018b, 2021).

The factors responsible for surface latent heat flux differences from -12 to 0 h are assessed by comparing moisture disequilibrium and near-surface wind speeds between RI and SI TCs. At all lead times, the moisture disequilibrium differences between RI and SI TCs are noisy and generally lack statistical significance (not shown), so we only present the near-surface wind speed differences. From -12 to 0 h, the 10 -m wind speed differences, albeit small in magnitude, are statistically significant predominantly in the downshear-right quadrant (Figs. 5a–c). There, near-surface wind speeds are about 2 m s^{-1} faster in RI TCs. This result contrasts somewhat with Nguyen et al. (2019), who examined dropsonde data for TCs in moderate shear. Their composites showed that 10 -m wind speed differences between RI and SI TCs were more pronounced upshear, although those differences lacked statistical significance. The storm translation speed and direction are not significantly different between RI and SI TCs at -12 and -6 h (not shown), so these parameters are not the cause of the wind speed differences.

A plausible hypothesis is that SI primes the inner core for subsequent RI, resulting in the higher initial intensities of RI

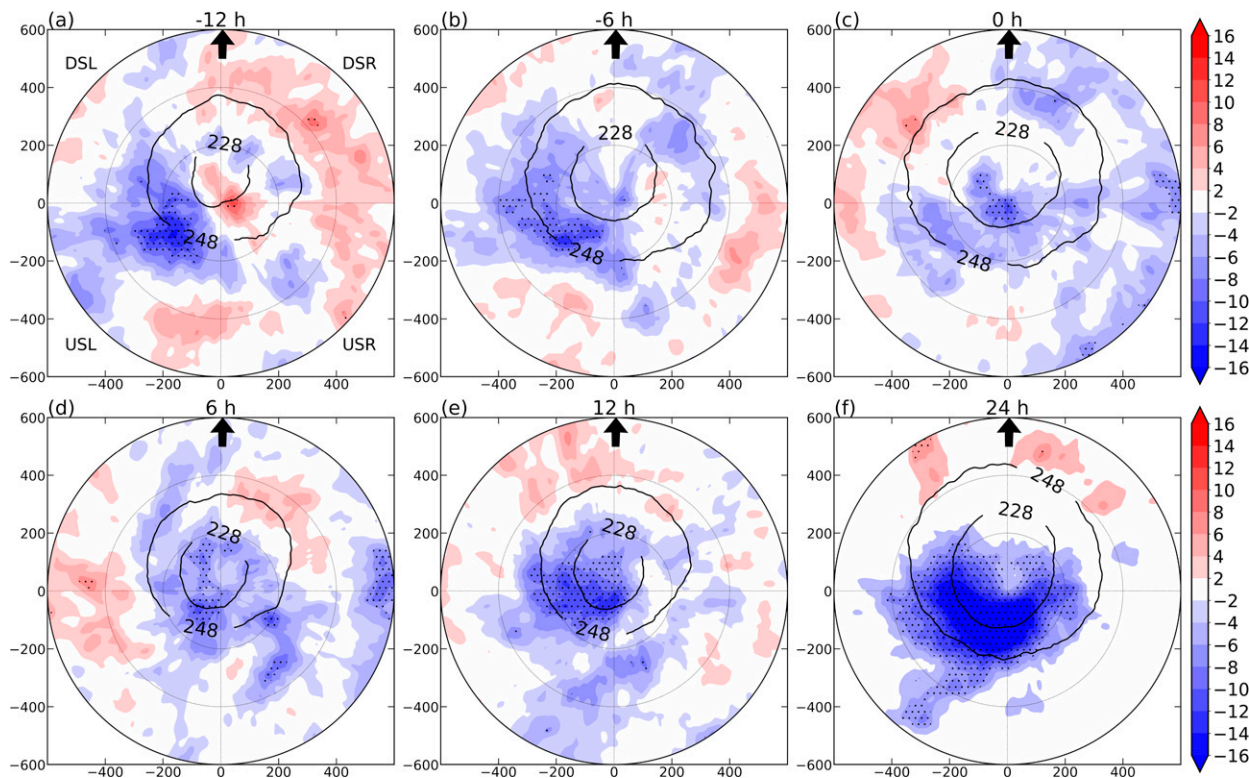


FIG. 8. As in Fig. 4, but for IR brightness temperatures (K).

TCs. Interestingly, in the North Atlantic, most RI TC analogs undergo a steady-state period (from -5 - to 5 -kt intensity change) in the 12-h period preceding RI onset (Fig. 2c), and the mean intensities of the two groups from -12 to -6 h are within 5 kt (Table 1). Moreover, sensitivity tests in which the RI sample was restricted to RI TCs that undergo a steady-state period from -12 to 0 h also revealed broader and slightly stronger near-surface wind fields in the RI TCs compared to analog SI TCs. Thus, the hypothesis that SI primes RI does not appear to be supported. It is instead hypothesized that differences in the near-surface wind field are indicative of structural characteristics that favor RI over SI in similar environments.

Areas of positive differences in near-surface wind speed (Fig. 5) generally overlap with areas of positive differences in surface latent heat fluxes (Fig. 4); however, there are noteworthy differences in the location of the greatest positive differences for each field prior to 0 h. At -12 h, the greatest positive differences in 10-m wind speed are mostly confined downshear (Fig. 5a), while the greatest positive surface latent heat flux differences are found in the left-of-shear quadrants (Fig. 4a). Similarly, at -6 h, the greatest positive differences in 10-m wind speed are mostly confined to the downshear-right quadrant (Fig. 5b), while large positive differences in surface latent flux are present in the left-of-shear and upshear quadrants (Fig. 4b). These difference patterns imply that, prior to 0 h, additional nonlinearly

interacting factors could contribute to the significantly larger surface fluxes in left-of-shear and upshear quadrants of RI TCs. After 6 h, the positive wind speed differences and surface latent heat flux differences in the inner core increase concurrently, as expected, indicative of the diverging intensification rates.

2) MOISTURE FLUX CONVERGENCE

As surface fluxes supply the TC boundary layer with moisture for convection, significant differences in surface latent heat flux patterns could also contribute to differences in the strength and areal coverage of moist convection between RI and SI TCs. Column-integrated horizontal moisture flux convergence (MFC) diagnoses where deep moist convection is likely present.

Figure 6 depicts the mean column-integrated horizontal MFC and the differences between RI and SI TCs. The mean MFC has an asymmetric distribution, characterized by a maximum located directly downshear of the TC center. Initially, the largest positive MFC differences are displaced cyclonically downwind of the downshear maximum in the composite mean, and the largest negative differences are located cyclonically upwind of the maximum. Additionally, the largest positive MFC differences tend to be located near, or just cyclonically downwind, of the largest positive surface latent heat flux differences.

After 0 h, the MFC of RI TCs evolves toward increasing azimuthal symmetry. This increasing symmetry is evidenced by the

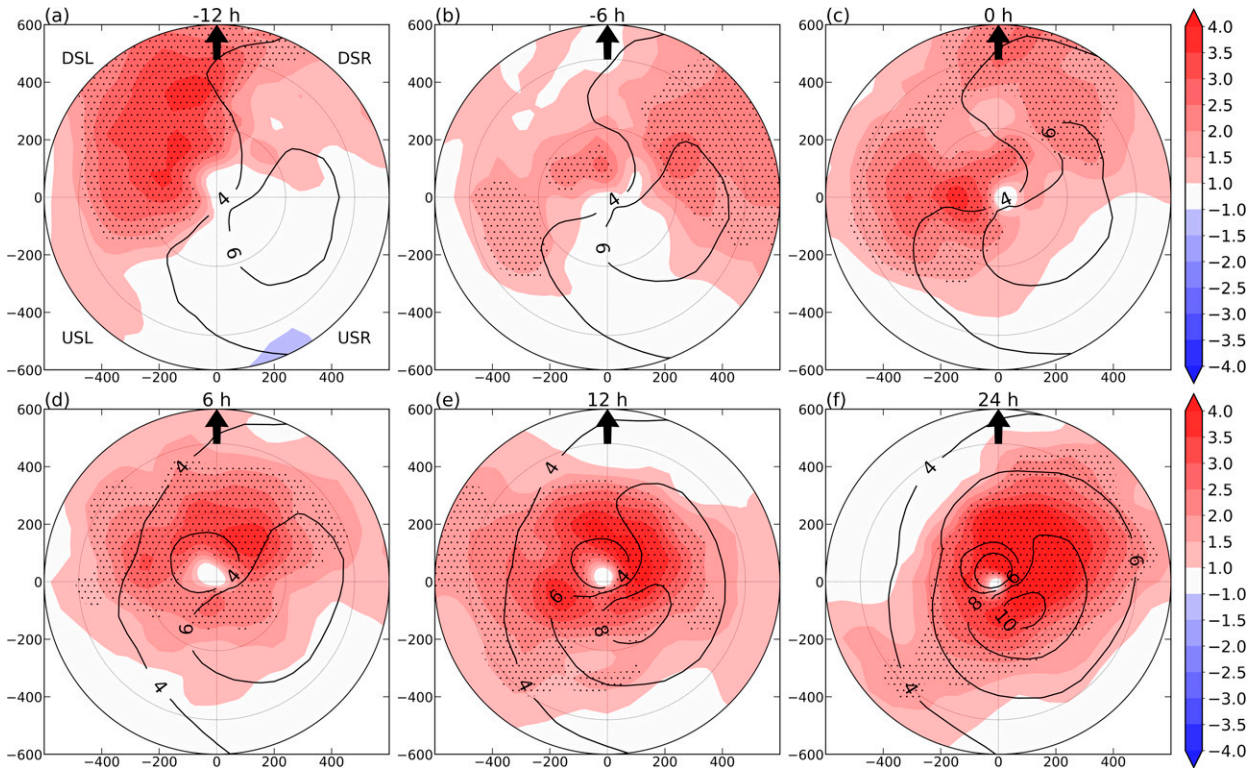


FIG. 9. As in Fig. 4, but for 400-hPa tangential wind composite differences (m s^{-1}).

shift of positive MFC differences from mostly the downshear-left quadrant to upshear. From the water budget equation, the column-integrated MFC is proportional to the column-integrated difference between condensation and evaporation, which is proportional to the net latent heat release. Thus, greater azimuthal symmetry of column-integrated MFC in RI TCs could be indicative of greater azimuthal symmetry of latent heating, which is the more favorable configuration for spin up of the vortex (Nolan et al. 2007).

3) TROPOSPHERIC MOISTURE

The tropospheric moisture content is also important for TC RI (e.g., Kaplan and DeMaria 2003; Kaplan et al. 2015; Wang and Jiang 2021), motivating further examination of the shear-relative locations and vertical layers with the largest moisture differences between RI and SI TCs. The total precipitable water composite differences and relative humidity composite differences below 500 hPa reveal no systematic differences between RI and SI TCs from -12 to 24 h (not shown). However, notable relative humidity differences are present around 400 hPa (Fig. 7). As early as -12 h, positive relative humidity differences of about 8% are present in the upshear-left quadrant, consistent with observational and modeling studies that demonstrated moistening in upshear quadrants prior to RI (e.g., Zawislak et al. 2016; Alvey et al. 2020).

From -6 to 0 h, a more symmetric relative humidity pattern emerges in RI TCs as positive differences of up to 5%

expand in areal coverage within the innermost 400 km of upshear quadrants (Figs. 7b,c). Although these positive differences upshear are relatively small in magnitude and are not statistically significant, they suggest increasing azimuthal symmetry of 400-hPa relative humidity ahead of RI onset, possibly promoting azimuthal symmetry of inner-core convection in RI TCs. By 24 h, the positive relative humidity differences in the innermost 400 km amplify to about 14% (Fig. 7f). Using a similar analog method, Rios-Berrios and Torn (2017) found that greater midtropospheric relative humidity, particularly in the upshear region, distinguishes intensifying TCs from steady-state TCs experiencing moderate vertical shear.

4) INFRARED BRIGHTNESS TEMPERATURES

The analysis above is complemented with an analysis of differences in convective characteristics between RI and SI TCs using composites of IR brightness temperatures (Fig. 8). At -12 h, the deepest convection (coldest IR brightness temperatures) occurs downshear of the TC center for both RI and SI TCs (Fig. 8a). This pronounced convective asymmetry in the composite mean is consistent with the effects of vertical wind shear on the TC convective structure (e.g., Corbosiero and Molinari 2002, 2003; Chen et al. 2006; Fischer et al. 2017). At -12 and -6 h, an area of significant, negative IR brightness temperature differences, approximately 10-K colder cloud tops in RI TCs, is present in the upshear-left quadrant (Figs. 8a,b). This finding is consistent with composites of Doppler radar data

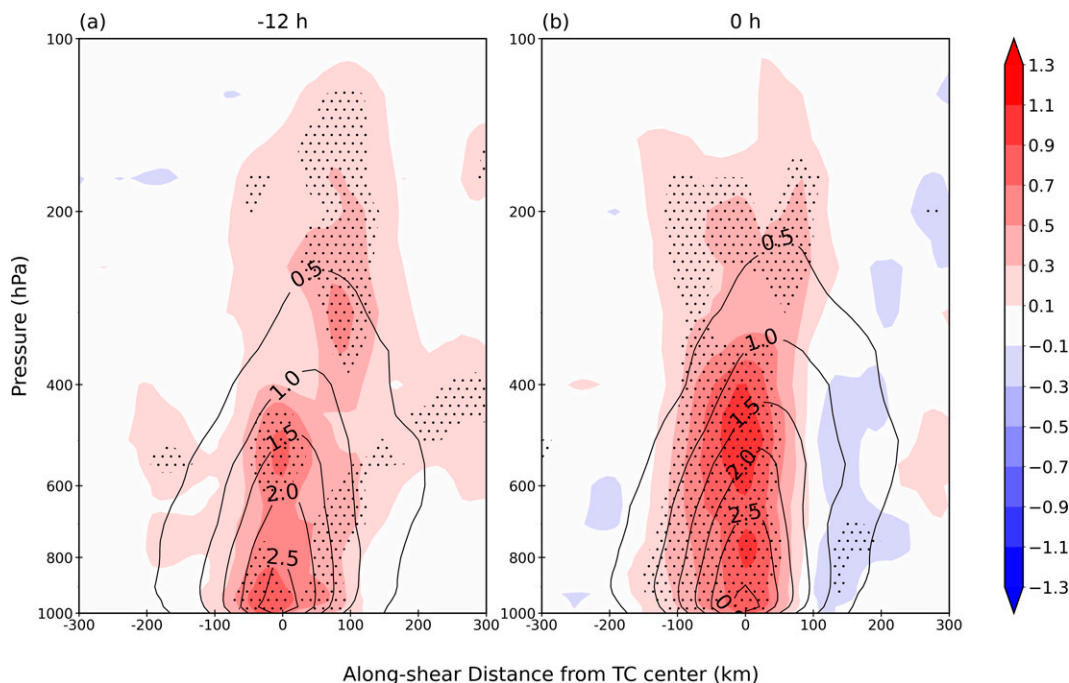


FIG. 10. TC-centered, along-shear vertical cross section of relative vorticity differences between analog RI and SI TCs (shaded; 10^{-4} s^{-1}) and mean of the combined RI and SI TC samples (contoured; 10^{-4} s^{-1}) in the North Atlantic at (a) -12 and (b) 0 h. The cross section spans 300 km from the TC center in both the upshear (negative values on the abscissa) and downshear (positive values on the abscissa) directions. Stippling indicates statistically significant differences at the 95% confidence interval.

over a 13-yr period by [Wadler et al. \(2018a\)](#) and ensemble simulations of Hurricane Edouard (2014) performed by [Leighton et al. \(2018\)](#), which showed that the migration of convective bursts from the downshear side to the upshear-left quadrant distinguished RI members from non-RI members.

After 0 h, the upshear expansion and subsequent amplification of negative IR brightness temperature differences are indicative of increasing azimuthal symmetry of deeper convection in RI TCs ([Figs. 8d–f](#)). These IR brightness temperature differences are in agreement with previous studies that related an increase in azimuthal coverage of precipitation to greater rates of intensification, including RI (e.g., [Zagrodnik and Jiang 2014](#); [Alvey et al. 2015](#); [Kaplan et al. 2015](#); [Tao and Jiang 2015](#); [Rios-Berrios and Torn 2017](#); [Tao et al. 2017](#); [Fischer et al. 2018](#); [Alvey et al. 2020](#)). Additionally, greater surface latent heat fluxes and MFC in left-of-shear and upshear quadrants, along with higher mid- to upper-tropospheric relative humidity upshear, would help promote increasing azimuthal symmetry of convection. The consistency between the IR brightness temperature differences and moisture field differences lends credibility to the ability of ERA5 to resolve the broad storm-scale differences between RI and SI TCs, along with some of the processes responsible for these differences.

5) KINEMATIC CHARACTERISTICS

In addition to the thermodynamic and cloud structure, the TC kinematic structure and evolution may also play a role in

favoring RI versus SI. Storm-relative tangential wind differences are positive through the troposphere (not shown) but are most pronounced near 400 hPa ([Fig. 9](#)). At this level, significant positive differences appear over a broad region around the TC from -12 to 0 h ([Figs. 9a–c](#)). The right-of-shear orientation of the maximum in the mean storm-relative tangential wind and left-of-shear orientation of the greatest positive differences indicate that RI TCs have a stronger, more symmetric circulation at mid- to upper levels prior to the intensity change period.

The larger tangential wind differences aloft from -12 to 0 h ([Figs. 9a–c](#)) point to differences between the vortex structures of RI and SI TCs, which are further analyzed using storm-centered, vertical cross sections of relative vorticity taken in the along-shear direction ([Fig. 10](#)). The mean vorticity structure generally displays a slight downshear tilt with height above the 700 -hPa level. Statistically significant, positive relative vorticity differences extend from the surface to above 200 hPa, and are maximized at the midlevels. Given that intensity differences between analogs are relatively small during this period ([Fig. 2b](#) and [Table 1](#)), the stronger and deeper mid- to upper-level vortex structure in RI TCs leading up to RI onset suggests the importance of the three-dimensional vortex structure to RI versus SI. By 0 h, the statistically significant positive relative vorticity differences at midlevels are mostly present to the left of the mean vorticity maximum axis ([Fig. 10b](#)), suggesting that RI TCs achieve a more vertically aligned vortex at RI onset. Recent studies have found

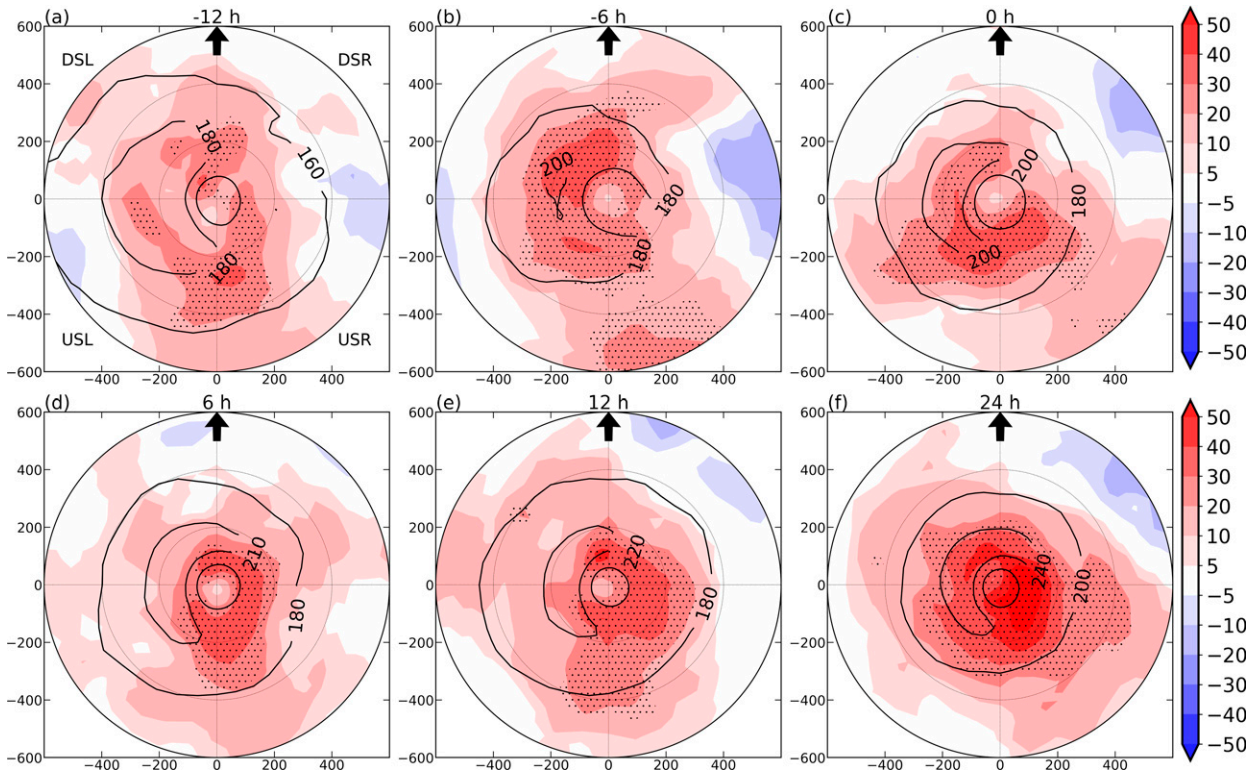


FIG. 11. As in Fig. 4, but for surface latent heat fluxes (W m^{-2}) for analog RI and SI TCs in the western North Pacific.

that alignment of the vortex is a key precursor to RI onset (e.g., Munsell et al. 2017; Miyamoto and Nolan 2018; Hazelton et al. 2020).

The initial strength, depth and vertical alignment of the vortex may be important to the rate of intensification for several reasons. A stronger, deeper, and more aligned vortex provides greater resiliency against shear (e.g., Hazelton et al. 2020; Finocchio and Rios-Berrios 2021) and intrusions of environmental air (Riemer and Montgomery 2011). Additionally, the stronger and more aligned vortex could potentially contribute to the midlevel humidification of upshear quadrants by circulating condensate into the upshear semicircle. For example, Alvey et al. (2020) showed that a more vertically aligned vortex favored horizontal water vapor advection from downshear-left to upshear-left quadrants at the mid- to upper levels, moistening the upshear environment and promoting greater symmetry of convection.

b. Western North Pacific

Tropical cyclone intensification in the North Atlantic may be influenced by characteristic features of this basin, which could result in unique RI pathways. To determine whether the factors associated with RI in the North Atlantic are generalizable, we compare analog RI and SI TCs in the western North Pacific basin. Figure 11 shows the evolution of the mean surface latent heat fluxes and composite differences

between TC analogs. As in the North Atlantic, surface latent heat fluxes tend to be maximized to the left of shear. RI TCs generally have significantly larger surface fluxes than SI TCs within the innermost 400 km. Prior to the onset of the intensity change period, significant positive differences of up to 40 W m^{-2} are present left of shear and upshear, within 200 km. Thereafter, positive differences are maximized upshear and right of shear, indicating greater azimuthal symmetry of surface latent heat fluxes in RI TCs versus SI TCs.

Surface latent heat flux differences are largely driven by 10-m wind speed differences, with RI TCs having a broader and stronger near-surface wind field (not shown). Although the analog algorithm attempts to match TCs based on initial intensity, RI TCs tend to have slightly higher initial intensities than SI TCs (Table 2), contributing to surface latent heat flux differences (Fig. 11). Yet, it is interesting to note that the preceding 12-h intensity change is not very different between SI and RI TCs (Fig. 2f). In fact, on average, SI TCs have slightly higher intensification rates from -12 to 0 h compared to RI TCs. Similar to the North Atlantic, the vortex structure as a whole appears to be important for RI versus SI. In RI TCs, the stronger and broader near-surface wind fields are reflected in the relative vorticity composite differences, which show positive differences over much of the troposphere near the center (Fig. 12). RI TCs exhibit a stronger vortex up to 200 hPa and are more vertically aligned at 0 h (Fig. 12b).

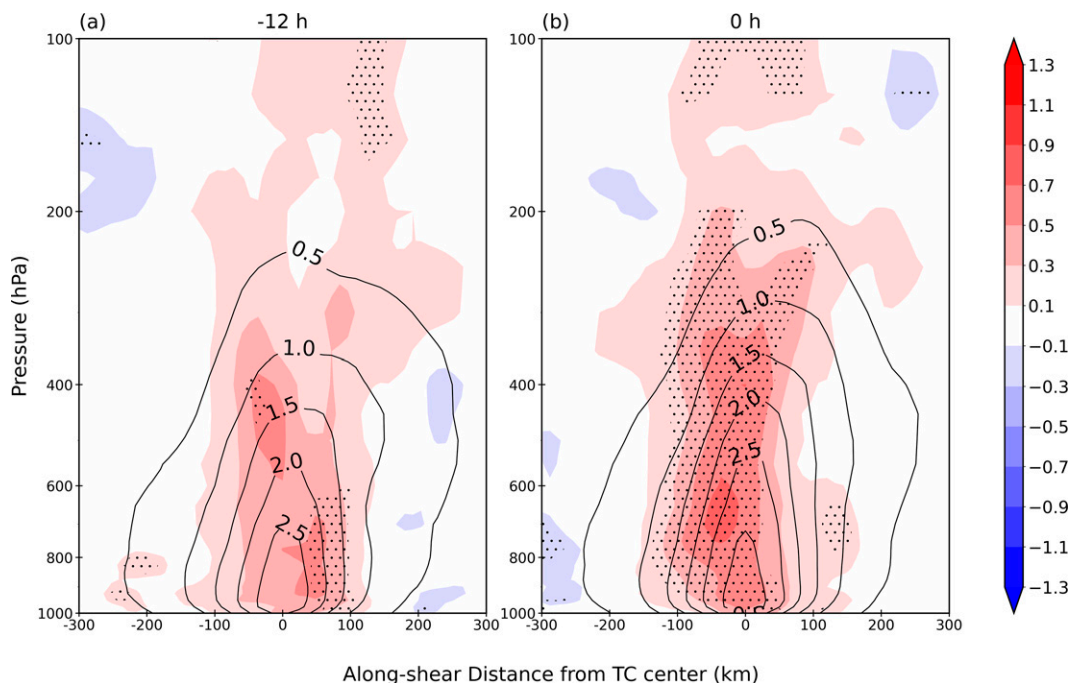


FIG. 12. As in Fig. 10, but for along-shear vertical cross section of relative vorticity (10^{-4} s^{-1}) for analog RI and SI TCs in the western North Pacific.

The differences in vortex structure could also contribute to differences in the relative humidity distribution about the TC. Similar to the North Atlantic, relative humidity differences are most pronounced around 400 hPa (Fig. 13). Although the 400-hPa relative humidity differences are not significant over a large region until 0 h, positive differences upshear-left, albeit small, are present at -12 and -6 h (Figs. 13a,b). At the onset of the intensity change period, RI TCs have as much as 8% greater 400-hPa relative humidity in the upshear-left quadrant (Fig. 13c). Subsequently, areas of significant positive relative humidity differences progress cyclonically downstream into the upshear-right quadrant and spread inward. The interbasin similarity between 400-hPa positive relative humidity differences in the upshear-left region suggests that mid- to upper-level humidification in this region prior to the intensity change period could be a relevant factor favoring RI versus SI. Additional research efforts, such as high-resolution modeling, are needed to assess the cause of these moisture differences and their importance to the intensification rate.

The larger surface latent heat fluxes in RI TCs persist over a broad region upshear from -12 to 0 h (Figs. 11a–c) and increase the supply of moisture and buoyancy to convection upshear, which can be examined through the IR brightness temperatures. A comparison of IR brightness temperatures reveals significant differences in convective intensity between RI and SI TCs (Fig. 14). At -12 h, an area of >10 K lower IR brightness temperatures, indicative of colder tops in RI TCs, is generally present to the left of shear and upshear within

200 km (Fig. 14a). From -12 to 0 h, this area of colder cloud tops is most prominent in the inner-core region of the upshear-left quadrant (Figs. 14a–c). Significantly lower brightness temperatures in RI TCs are collocated with the composite mean convective maximum at 0 h, reflecting higher initial intensities of RI TCs relative to SI TCs in this basin (Fig. 2d). The subsequent amplification and expansion of negative IR brightness temperature differences upshear is again consistent with 400-hPa relative humidity differences. Overall, the consistency between the evolution of IR brightness temperature differences in the North Atlantic and western North Pacific basins indicates that RI is associated with increasing azimuthal symmetry of convection beginning prior to, and continuing throughout, the intensity change period.

It is worth noting that the evolution of brightness temperature differences between analog RI and SI TCs in the eastern North Pacific (not shown) is strongly consistent with the results shown in the western North Pacific and North Atlantic. In contrast, composites differences between ERA5 fields associated with analog RI and SI TCs in the eastern North Pacific were muted throughout the 24-h intensification period, suggesting that the ERA5 is limited in its ability to adequately resolve the broadscale structure of eastern North Pacific TCs. Such limitations could be partially attributed to the smaller than average size of eastern North Pacific TCs relative to TCs in other basins (Knaff et al. 2014).

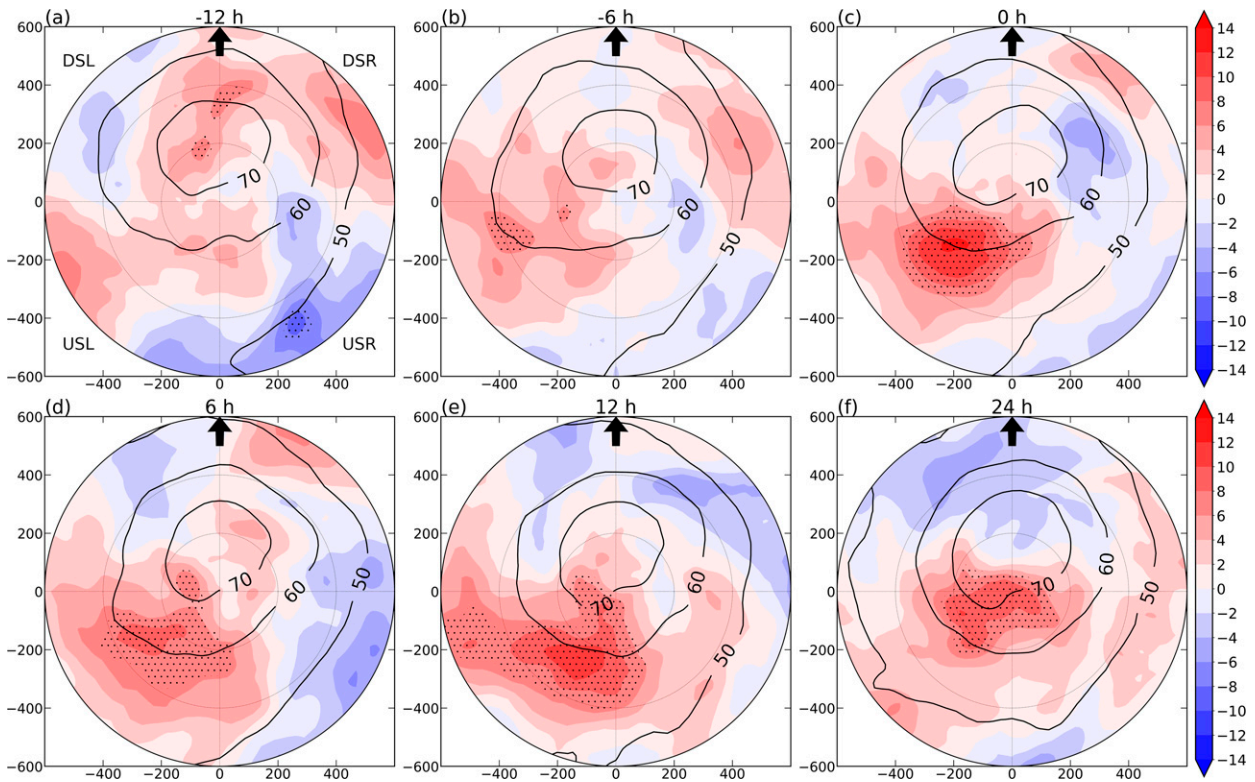


FIG. 13. As in Fig. 7, but for 400-hPa relative humidity (%) for analog RI and SI TCs in the western North Pacific.

4. Discussion and conclusions

This study examined environmental and storm-scale characteristics of RI and SI TCs in the North Atlantic and western North Pacific using the ERA5 and GridSat datasets. In contrast to previous statistical analyses of RI, an analog method was employed to control for three factors that influence TC intensity change: initial intensity, MPI, and vertical wind shear. The effects of these three parameters are likely conflated in prior studies. Composite fields of analog RI and SI TCs were compared in the hours leading up to and during the 24-h intensity change period to evaluate differences between RI and SI TCs.

The main differences between RI and SI TC analogs, which were statistically significant prior to and during the 24-h intensity change period, are summarized in Fig. 15. Near the onset of the intensity change period, RI TCs have a stronger and deeper vortex that achieves a more upright structure, as well as colder IR brightness temperatures upshear, indicative of more symmetric convection around the center. A more aligned and intense vortex at or near RI onset is consistent with the results of prior observational case studies and simulations (e.g., Stevenson et al. 2014; Rogers et al. 2015; Munsell et al. 2017; Chen et al. 2018; Leighton et al. 2018; Miyamoto and Nolan 2018; Alvey et al. 2020), and is more resilient to ventilation by shear (e.g., Reasor et al. 2004; Reasor and Eastin 2012). As the azimuthal coverage of convection in the inner core increases, the more upright vortex concentrates

strong axisymmetric latent heating within the region of high inertial stability, increasing the efficiency of the conversion of available potential energy to kinetic energy (e.g., Nolan et al. 2007; Vigh and Schubert 2009) and promoting faster spin-up of the TC vortex. Additionally, the stronger, more vertically aligned vortex prior to the intensity change period can also potentially contribute to the moistening of upshear quadrants at mid- to upper levels, through the horizontal advection of condensate and moisture from the downshear-left to upshear-left quadrants (Alvey et al. 2020).

Stronger and more symmetric surface latent heat fluxes also differentiate RI TCs from SI TCs. Larger surface latent heat fluxes in RI TCs is primarily attributed to a stronger near-surface wind field. Prior modeling and observational studies have found that a more symmetric pattern of surface latent heat fluxes is associated with faster rates of TC intensification (e.g., Rappin and Nolan 2012; Onderlinde and Nolan 2016; Gao et al. 2016; Rios-Berrios and Torn 2017; Nguyen et al. 2019; Wadler et al. 2018b, 2021). The enhanced left-of-shear and upshear surface latent heat fluxes, together with enhanced left-of-shear column-integrated horizontal moisture flux convergence, may promote the persistence and invigoration of upshear convection in RI TCs.

By controlling for the initial intensity, the vertical wind shear, and the MPI, RI and SI TCs have other thermodynamic, convective, and kinematic differences that appear useful for assessing the favorability for RI. It should be noted

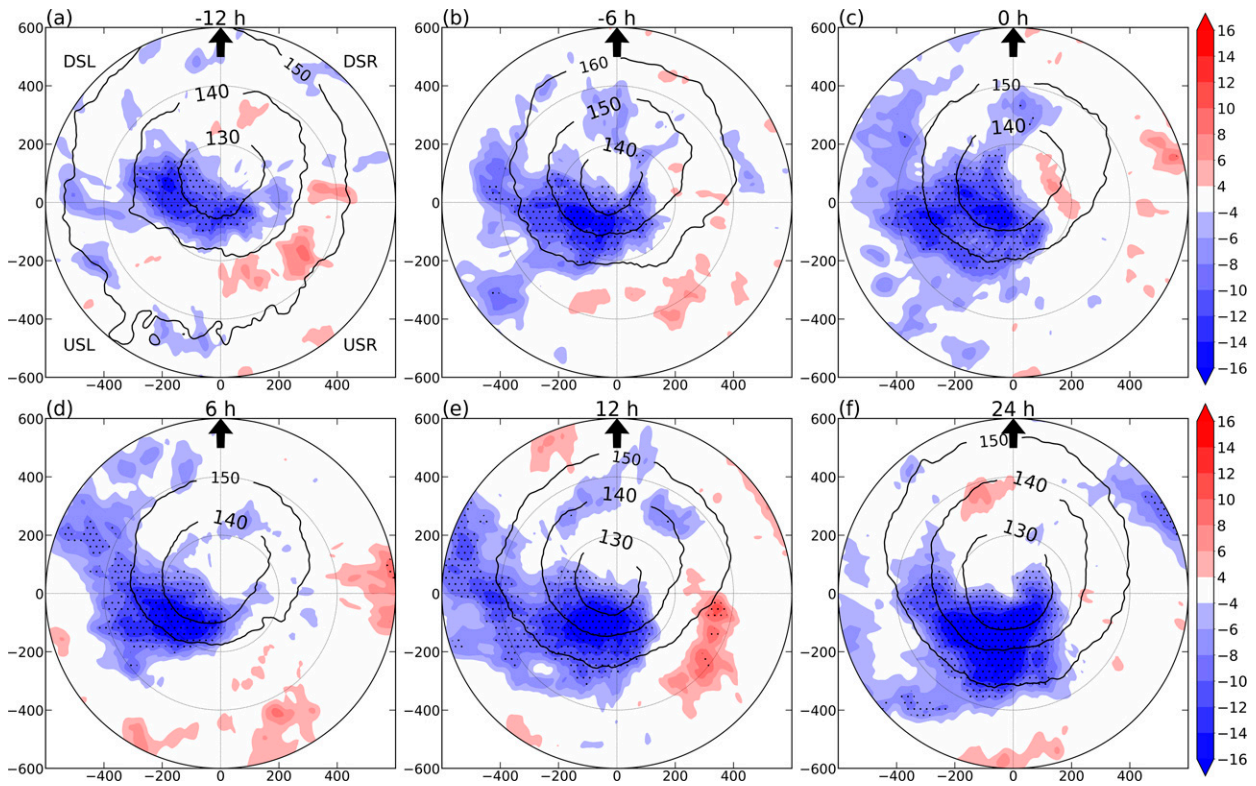


FIG. 14. As in Fig. 8, but for IR brightness temperatures (K) for analog RI and SI TCs in the western North Pacific.

that a high-resolution modeling framework is needed to support the vortex tilt evolution leading up to RI versus SI. Although the relatively coarse ERA5 resolution is a limitation, the broad environmental and storm-scale differences between RI and SI TCs are consistent with the convective evolution differences and support the finding that processes that aid in

increasing the azimuthal symmetry of inner-core convection support RI. Additional research, using this analog framework, case studies, observations, and high-resolution model simulations would be useful for further exploring differences between RI and SI TCs and linking together relevant processes leading to RI.

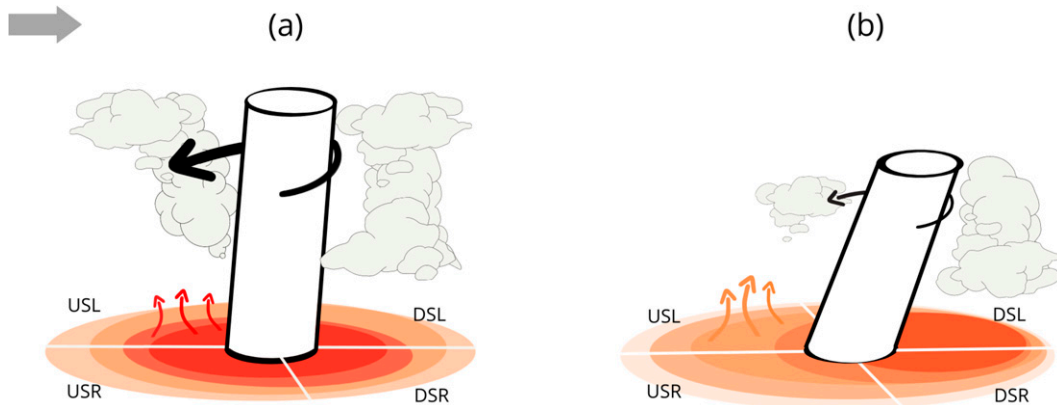


FIG. 15. Schematic demonstrating the key differences between analog (a) RI and (b) SI TCs at the start of the intensity change period (0 h). Compared to SI TCs, RI TCs have a stronger, deeper, more vertically aligned vortex (cylinder), stronger mid- to upper-level tangential winds (black arrow), greater azimuthal symmetry of surface latent heat fluxes (red shading) with larger fluxes to the left of shear and upshear (red arrows), and deeper convection left of shear and upshear (clouds). The gray arrow denotes the vertical wind shear direction, and shear-relative quadrants are labeled.

Acknowledgments. This research was supported by the Office of Naval Research Grants N000141712714 and N000142012057. The authors thank Haiyan Jiang and two anonymous reviewers for their constructive comments and suggestions, which helped improve the quality of the manuscript.

Data availability statement. Tropical cyclone best track data used in this study are available from NOAA's International Best Track Archive for Climate Stewardship (IBTrACS) data, accessed on 11 June 2021. ERA5 data are available through the Climate Data Store at <https://cds.climate.copernicus.eu>. The GridSat-B1 data are openly available from NOAA's National Centers for Environmental Information at <https://www.ncdc.noaa.gov/gibbs/>.

REFERENCES

- Alland, J. J., B. H. Tang, K. L. Corbosiero, and G. H. Bryan, 2021a: Combined effects of midlevel dry air and vertical wind shear on tropical cyclone development. Part I: Downdraft ventilation. *J. Atmos. Sci.*, **78**, 763–782, <https://doi.org/10.1175/JAS-D-20-0054.1>.
- , —, —, and —, 2021b: Combined effects of midlevel dry air and vertical wind shear on tropical cyclone development. Part II: Radial ventilation. *J. Atmos. Sci.*, **78**, 783–796, <https://doi.org/10.1175/JAS-D-20-0055.1>.
- Alvey, G. R., J. Zawislak, and E. Zipser, 2015: Precipitation properties observed during tropical cyclone intensity change. *Mon. Wea. Rev.*, **143**, 4476–4492, <https://doi.org/10.1175/MWR-D-15-0065.1>.
- , E. Zipser, and J. Zawislak, 2020: How does Hurricane Edouard (2014) evolve toward symmetry before rapid intensification? A high-resolution ensemble study. *J. Atmos. Sci.*, **77**, 1329–1351, <https://doi.org/10.1175/JAS-D-18-0355.1>.
- Bhatia, K. T., and D. S. Nolan, 2013: Relating the skill of tropical cyclone intensity forecasts to the synoptic environment. *Wea. Forecasting*, **28**, 961–980, <https://doi.org/10.1175/WAF-D-12-00110.1>.
- Chen, H., and S. G. Gopalakrishnan, 2015: A study on the asymmetric rapid intensification of Hurricane Earl (2010) using the HWRF system. *J. Atmos. Sci.*, **72**, 531–550, <https://doi.org/10.1175/JAS-D-14-0097.1>.
- Chen, S. S., J. A. Knaff, and F. D. Marks, 2006: Effects of vertical wind shear and storm motion on tropical cyclone rainfall asymmetries deduced from TRMM. *Mon. Wea. Rev.*, **134**, 3190–3208, <https://doi.org/10.1175/MWR3245.1>.
- Chen, X., Y. Wang, J. Fang, and M. Xue, 2018: A numerical study on rapid intensification of Typhoon Vicente (2012) in the South China Sea. Part II: Roles of inner-core processes. *J. Atmos. Sci.*, **75**, 235–255, <https://doi.org/10.1175/JAS-D-17-0129.1>.
- Corbosiero, K. L., and J. Molinari, 2002: The effects of vertical wind shear on the distribution of convection in tropical cyclones. *Mon. Wea. Rev.*, **130**, 2110–2123, [https://doi.org/10.1175/1520-0493\(2002\)130<2110:TEOVWS>2.0.CO;2](https://doi.org/10.1175/1520-0493(2002)130<2110:TEOVWS>2.0.CO;2).
- , and —, 2003: The relationship between storm motion, vertical wind shear, and convective asymmetries in tropical cyclones. *J. Atmos. Sci.*, **60**, 366–376, [https://doi.org/10.1175/1520-0469\(2003\)060<0366:TRBSMV>2.0.CO;2](https://doi.org/10.1175/1520-0469(2003)060<0366:TRBSMV>2.0.CO;2).
- Dee, D. P., and Coauthors, 2011: The ERA-Interim reanalysis: Configuration and performance of the data assimilation system. *Quart. J. Roy. Meteor. Soc.*, **137**, 553–597, <https://doi.org/10.1002/qj.828>.
- DeMaria, M., M. Mainelli, L. K. Shay, J. A. Knaff, and J. Kaplan, 2005: Further improvements to the Statistical Hurricane Intensity Prediction Scheme (SHIPS). *Wea. Forecasting*, **20**, 531–543, <https://doi.org/10.1175/WAF862.1>.
- , C. R. Sampson, J. A. Knaff, and K. D. Musgrave, 2014: Is tropical cyclone intensity guidance improving? *Bull. Amer. Meteor. Soc.*, **95**, 387–398, <https://doi.org/10.1175/BAMS-D-12-00240.1>.
- Dullaart, J. C. M., S. Muis, N. Bloemendaal, and J. C. J. H. Aerts, 2020: Advancing global storm surge modelling using the new ERA5 climate reanalysis. *Climate Dyn.*, **54**, 1007–1021, <https://doi.org/10.1007/s00382-019-05044-0>.
- Emanuel, K., C. DesAutels, C. Holloway, and R. Korty, 2004: Environmental control of tropical cyclone intensity. *J. Atmos. Sci.*, **61**, 843–858, [https://doi.org/10.1175/1520-0469\(2004\)061<0843:ECOTCI>2.0.CO;2](https://doi.org/10.1175/1520-0469(2004)061<0843:ECOTCI>2.0.CO;2).
- Finocchio, P. M., and S. J. Majumdar, 2017: The predictability of idealized tropical cyclones in environments with time-varying vertical wind shear. *J. Adv. Model. Earth Syst.*, **9**, 2836–2862, <https://doi.org/10.1002/2017MS001168>.
- , and R. Rios-Berrios, 2021: The intensity- and size-dependent response of tropical cyclones to increasing vertical wind shear. *J. Atmos. Sci.*, **78**, 3673–3690, <https://doi.org/10.1175/JAS-D-21-0126.1>.
- , S. J. Majumdar, D. S. Nolan, and M. Iskandarani, 2016: Idealized tropical cyclone responses to the height and depth of environmental vertical wind shear. *Mon. Wea. Rev.*, **144**, 2155–2175, <https://doi.org/10.1175/MWR-D-15-0320.1>.
- Fischer, M. S., B. H. Tang, and K. L. Corbosiero, 2017: Assessing the influence of upper-tropospheric troughs on tropical cyclone intensification rates after genesis. *Mon. Wea. Rev.*, **145**, 1295–1313, <https://doi.org/10.1175/MWR-D-16-0275.1>.
- , —, —, and C. M. Rozoff, 2018: Normalized convective characteristics of tropical cyclone rapid intensification events in the North Atlantic and eastern North Pacific. *Mon. Wea. Rev.*, **146**, 1133–1155, <https://doi.org/10.1175/MWR-D-17-0239.1>.
- , —, and —, 2019: A climatological analysis of tropical cyclone rapid intensification in environments of upper-tropospheric troughs. *Mon. Wea. Rev.*, **147**, 3693–3719, <https://doi.org/10.1175/MWR-D-19-0013.1>.
- Frank, W. M., and E. A. Ritchie, 2001: Effects of vertical wind shear on the intensity and structure of numerically simulated hurricanes. *Mon. Wea. Rev.*, **129**, 2249–2269, [https://doi.org/10.1175/1520-0493\(2001\)129<2249:EOVWSO>2.0.CO;2](https://doi.org/10.1175/1520-0493(2001)129<2249:EOVWSO>2.0.CO;2).
- Gao, S., S. Zhai, L. S. Chiu, and D. Xia, 2016: Satellite air–sea enthalpy flux and intensity change of tropical cyclones over the western North Pacific. *J. Appl. Meteor. Climatol.*, **55**, 425–444, <https://doi.org/10.1175/JAMC-D-15-0171.1>.
- Gray, W. M., 1968: Global view of the origin of tropical disturbances and storms. *Mon. Wea. Rev.*, **96**, 669–700, [https://doi.org/10.1175/1520-0493\(1968\)096<0669:GVOTOO>2.0.CO;2](https://doi.org/10.1175/1520-0493(1968)096<0669:GVOTOO>2.0.CO;2).
- Halperin, D. J., and R. D. Torn, 2018: Diagnosing conditions associated with large intensity forecast errors in the Hurricane Weather Research and Forecasting (HWRF) Model. *Wea. Forecasting*, **33**, 239–266, <https://doi.org/10.1175/WAF-D-17-0077.1>.
- Hazelton, A. T., X. Zhang, S. Gopalakrishnan, W. Ramstrom, F. Marks, and J. A. Zhang, 2020: High-resolution ensemble HFV3 forecasts of Hurricane Michael (2018): Rapid intensification in shear. *Mon. Wea. Rev.*, **148**, 2009–2032, <https://doi.org/10.1175/MWR-D-19-0275.1>.
- Hence, D. A., and R. A. Houze, 2012: Vertical structure of tropical cyclone rainbands as seen by the TRMM Precipitation

- Radar. *J. Atmos. Sci.*, **69**, 2644–2661, <https://doi.org/10.1175/JAS-D-11-0323.1>.
- Hendricks, E. A., M. S. Peng, B. Fu, and T. Li, 2010: Quantifying environmental control on tropical cyclone intensity change. *Mon. Wea. Rev.*, **138**, 3243–3271, <https://doi.org/10.1175/2010MWR3185.1>.
- Hersbach, H., and Coauthors, 2020: The ERA5 global reanalysis. *Quart. J. Roy. Meteor. Soc.*, **146**, 1999–2049, <https://doi.org/10.1002/qj.3803>.
- Hodges, K., A. Cobb, and P. L. Vidale, 2017: How well are tropical cyclones represented in reanalysis datasets? *J. Climate*, **30**, 5243–5264, <https://doi.org/10.1175/JCLI-D-16-0557.1>.
- Jaimes, B., L. K. Shay, and E. W. Uhlhorn, 2015: Enthalpy and momentum fluxes during Hurricane Earl relative to underlying ocean features. *Mon. Wea. Rev.*, **143**, 111–131, <https://doi.org/10.1175/MWR-D-13-00277.1>.
- Judt, F., and S. S. Chen, 2016: Predictability and dynamics of tropical cyclone rapid intensification deduced from high-resolution stochastic ensembles. *Mon. Wea. Rev.*, **144**, 4395–4420, <https://doi.org/10.1175/MWR-D-15-0413.1>.
- Kaplan, J., and M. DeMaria, 1995: A simple empirical model for predicting the decay of tropical cyclone winds after landfall. *J. Appl. Meteor.*, **34**, 2499–2512, [https://doi.org/10.1175/1520-0450\(1995\)034<2499:ASEMFP>2.0.CO;2](https://doi.org/10.1175/1520-0450(1995)034<2499:ASEMFP>2.0.CO;2).
- , and —, 2003: Large-scale characteristics of rapidly intensifying tropical cyclones in the North Atlantic basin. *Wea. Forecasting*, **18**, 1093–1108, [https://doi.org/10.1175/1520-0434\(2003\)018<1093:LCORIT>2.0.CO;2](https://doi.org/10.1175/1520-0434(2003)018<1093:LCORIT>2.0.CO;2).
- , —, and J. A. Knaff, 2010: A revised tropical cyclone rapid intensification index for the Atlantic and eastern North Pacific basins. *Wea. Forecasting*, **25**, 220–241, <https://doi.org/10.1175/2009WAF2222280.1>.
- , and Coauthors, 2015: Evaluating environmental impacts on tropical cyclone rapid intensification predictability utilizing statistical models. *Wea. Forecasting*, **30**, 1374–1396, <https://doi.org/10.1175/WAF-D-15-0032.1>.
- Kieper, M. E., and H. Jiang, 2012: Predicting tropical cyclone rapid intensification using the 37 GHz ring pattern identified from passive microwave measurements. *Geophys. Res. Lett.*, **39**, L13804, <https://doi.org/10.1029/2012GL052115>.
- Knaff, J. A., S. P. Longmore, and D. A. Molenaar, 2014: An objective satellite-based tropical cyclone size climatology. *J. Climate*, **27**, 455–476, <https://doi.org/10.1175/JCLI-D-13-00096.1>.
- Knapp, K. R., M. C. Kruk, D. H. Levinson, H. J. Diamond, and C. J. Neumann, 2010: The International Best Track Archive for Climate Stewardship (IBTrACS) unifying tropical cyclone data. *Bull. Amer. Meteor. Soc.*, **91**, 363–376, <https://doi.org/10.1175/2009BAMS2755.1>.
- , and Coauthors, 2011: Globally gridded satellite observations for climate studies. *Bull. Amer. Meteor. Soc.*, **92**, 893–907, <https://doi.org/10.1175/2011BAMS3039.1>.
- Landsea, C. W., and J. L. Franklin, 2013: Atlantic hurricane database uncertainty and presentation of a new database format. *Mon. Wea. Rev.*, **141**, 3576–3592, <https://doi.org/10.1175/MWR-D-12-00254.1>.
- Leighton, H., S. Gopalakrishnan, J. A. Zhang, R. F. Rogers, Z. Zhang, and V. Tallapragada, 2018: Azimuthal distribution of deep convection, environmental factors, and tropical cyclone rapid intensification: A perspective from HWRP ensemble forecasts of Hurricane Edouard (2014). *J. Atmos. Sci.*, **75**, 275–295, <https://doi.org/10.1175/JAS-D-17-0171.1>.
- Miyamoto, Y., and D. S. Nolan, 2018: Structural changes preceding rapid intensification in tropical cyclones as shown in a large ensemble of idealized simulations. *J. Atmos. Sci.*, **75**, 555–569, <https://doi.org/10.1175/JAS-D-17-0177.1>.
- Molinari, J., and D. Vollaro, 2010: Rapid intensification of a sheared tropical storm. *Mon. Wea. Rev.*, **138**, 3869–3885, <https://doi.org/10.1175/2010MWR3378.1>.
- Munsell, E. B., F. Zhang, J. A. Sippel, S. A. Braun, and Y. Weng, 2017: Dynamics and predictability of the intensification of Hurricane Edouard (2014). *J. Atmos. Sci.*, **74**, 573–595, <https://doi.org/10.1175/JAS-D-16-0018.1>.
- Nguyen, L. T., and J. Molinari, 2012: Rapid intensification of a sheared, fast-moving hurricane over the Gulf Stream. *Mon. Wea. Rev.*, **140**, 3361–3378, <https://doi.org/10.1175/MWR-D-11-00293.1>.
- , R. F. Rogers, and P. D. Reasor, 2017: Thermodynamic and kinematic influences on precipitation symmetry in sheared tropical cyclones: Bertha and Cristobal (2014). *Mon. Wea. Rev.*, **145**, 4423–4446, <https://doi.org/10.1175/MWR-D-17-0073.1>.
- , R. Rogers, J. Zawislak, and J. A. Zhang, 2019: Assessing the influence of convective downdrafts and surface enthalpy fluxes on tropical cyclone intensity change in moderate vertical wind shear. *Mon. Wea. Rev.*, **147**, 3519–3534, <https://doi.org/10.1175/MWR-D-18-0461.1>.
- Nolan, D. S., and L. D. Grasso, 2003: Nonhydrostatic, three-dimensional perturbations to balanced, hurricane-like vortices. Part II: Symmetric response and nonlinear simulations. *J. Atmos. Sci.*, **60**, 2717–2745, [https://doi.org/10.1175/1520-0469\(2003\)060<2717:NTPTBH>2.0.CO;2](https://doi.org/10.1175/1520-0469(2003)060<2717:NTPTBH>2.0.CO;2).
- , Y. Moon, and D. P. Stern, 2007: Tropical cyclone intensification from asymmetric convection: Energetics and efficiency. *J. Atmos. Sci.*, **64**, 3377–3405, <https://doi.org/10.1175/JAS3988.1>.
- Onderlinde, M. J., and D. S. Nolan, 2016: Tropical cyclone–relative environmental helicity and the pathways to intensification in shear. *J. Atmos. Sci.*, **73**, 869–890, <https://doi.org/10.1175/JAS-D-15-0261.1>.
- Pendergrass, A. G., and H. E. Willoughby, 2009: Diabatically induced secondary flows in tropical cyclones. Part I: Quasi-steady forcing. *Mon. Wea. Rev.*, **137**, 805–821, <https://doi.org/10.1175/2008MWR2657.1>.
- Rappin, E. D., and D. S. Nolan, 2012: The effect of vertical shear orientation on tropical cyclogenesis. *Quart. J. Roy. Meteor. Soc.*, **138**, 1035–1054, <https://doi.org/10.1002/qj.977>.
- Reasor, P. D., and M. D. Eastin, 2012: Rapidly intensifying Hurricane Guillermo (1997). Part II: Resilience in shear. *Mon. Wea. Rev.*, **140**, 425–444, <https://doi.org/10.1175/MWR-D-11-00080.1>.
- , M. T. Montgomery, and L. D. Grasso, 2004: A new look at the problem of tropical cyclones in vertical shear flow: Vortex resiliency. *J. Atmos. Sci.*, **61**, 3–22, [https://doi.org/10.1175/1520-0469\(2004\)061<0003:ANLATP>2.0.CO;2](https://doi.org/10.1175/1520-0469(2004)061<0003:ANLATP>2.0.CO;2).
- , R. Rogers, and S. Lorsolo, 2013: Environmental flow impacts on tropical cyclone structure diagnosed from airborne Doppler radar composites. *Mon. Wea. Rev.*, **141**, 2949–2969, <https://doi.org/10.1175/MWR-D-12-00334.1>.
- Riehl, H., and J. Malkus, 1961: Some aspects of Hurricane Daisy, 1958. *Tellus*, **13**, 181–213, <https://doi.org/10.3402/tellusa.v13i2.9495>.
- Riemer, M., and M. T. Montgomery, 2011: Simple kinematic models for the environmental interaction of tropical cyclones in vertical wind shear. *Atmos. Chem. Phys.*, **11**, 9395–9414, <https://doi.org/10.5194/acp-11-9395-2011>.
- , —, and M. E. Nicholls, 2010: A new paradigm for intensification modification of tropical cyclones: Thermodynamic impact

- of vertical wind shear on the inflow layer. *Atmos. Chem. Phys.*, **10**, 3163–3188, <https://doi.org/10.5194/acp-10-3163-2010>.
- , —, and —, 2013: Further examination of the thermodynamic modification of the inflow layer of tropical cyclones by vertical wind shear. *Atmos. Chem. Phys.*, **13**, 327–346, <https://doi.org/10.5194/acp-13-327-2013>.
- Rios-Berrios, R., and R. D. Torn, 2017: Climatological analysis of tropical cyclone intensity changes under moderate vertical wind shear. *Mon. Wea. Rev.*, **145**, 1717–1738, <https://doi.org/10.1175/MWR-D-16-0350.1>.
- , —, and C. A. Davis, 2016: An ensemble approach to investigate tropical cyclone intensification in sheared environments. Part I: Katia (2011). *J. Atmos. Sci.*, **73**, 71–93, <https://doi.org/10.1175/JAS-D-15-0052.1>.
- , C. A. Davis, and R. D. Torn, 2018: A hypothesis for the intensification of tropical cyclones under moderate vertical wind shear. *J. Atmos. Sci.*, **75**, 4149–4173, <https://doi.org/10.1175/JAS-D-18-0070.1>.
- Rogers, R., P. Reasor, and S. Lorsolo, 2013: Airborne Doppler observations of the inner-core structural differences between intensifying and steady-state tropical cyclones. *Mon. Wea. Rev.*, **141**, 2970–2991, <https://doi.org/10.1175/MWR-D-12-00357.1>.
- , —, and J. A. Zhang, 2015: Multiscale structure and evolution of Hurricane Earl (2010) during rapid intensification. *Mon. Wea. Rev.*, **143**, 536–562, <https://doi.org/10.1175/MWR-D-14-00175.1>.
- , J. A. Zhang, J. Zawislak, H. Jiang, G. R. Alvey III, E. J. Zipser, and S. N. Stevenson, 2016: Observations of the structure and evolution of Hurricane Edouard (2014) during intensity change. Part II: Kinematic structure and the distribution of deep convection. *Mon. Wea. Rev.*, **144**, 3355–3376, <https://doi.org/10.1175/MWR-D-16-0017.1>.
- Rozoff, C. M., and J. P. Kossin, 2011: New probabilistic forecast models for the prediction of tropical cyclone rapid intensification. *Wea. Forecasting*, **26**, 677–689, <https://doi.org/10.1175/WAF-D-10-05059.1>.
- , C. S. Velden, J. Kaplan, J. P. Kossin, and A. J. Wimmers, 2015: Improvements in the probabilistic prediction of tropical cyclone rapid intensification with passive microwave observations. *Wea. Forecasting*, **30**, 1016–1038, <https://doi.org/10.1175/WAF-D-14-00109.1>.
- Rygllicki, D. R., J. H. Cossuth, D. Hodyss, and J. D. Doyle, 2018a: The unexpected rapid intensification of tropical cyclones in moderate vertical wind shear. Part I: Overview and observations. *Mon. Wea. Rev.*, **146**, 3773–3800, <https://doi.org/10.1175/MWR-D-18-0020.1>.
- , J. D. Doyle, Y. Jin, D. Hodyss, and J. H. Cossuth, 2018b: The unexpected rapid intensification of tropical cyclones in moderate vertical wind shear. Part II: Vortex tilt. *Mon. Wea. Rev.*, **146**, 3801–3825, <https://doi.org/10.1175/MWR-D-18-0021.1>.
- Schenkel, B. A., and R. E. Hart, 2012: An examination of tropical cyclone position, intensity, and intensity life cycle within atmospheric reanalysis datasets. *J. Climate*, **25**, 3453–3475, <https://doi.org/10.1175/2011JCLI4208.1>.
- Shimada, U., K. Aonashi, and Y. Miyamoto, 2017: Tropical cyclone intensity change and axisymmetry deduced from GSMaP. *Mon. Wea. Rev.*, **145**, 1003–1017, <https://doi.org/10.1175/MWR-D-16-0244.1>.
- Stevenson, S. N., K. L. Corbosiero, and J. Molinari, 2014: The convective evolution and rapid intensification of Hurricane Earl (2010). *Mon. Wea. Rev.*, **142**, 4364–4380, <https://doi.org/10.1175/MWR-D-14-00078.1>.
- Tang, B., and K. Emanuel, 2010: Midlevel ventilation's constraint on tropical cyclone intensity. *J. Atmos. Sci.*, **67**, 1817–1830, <https://doi.org/10.1175/2010JAS3318.1>.
- Tao, C., and H. Jiang, 2015: Distributions of shallow to very deep precipitation–convection in rapidly intensifying tropical cyclones. *J. Climate*, **28**, 8791–8824, <https://doi.org/10.1175/JCLI-D-14-00448.1>.
- , —, and J. Zawislak, 2017: The relative importance of stratiform and convective rainfall in rapidly intensifying tropical cyclones. *Mon. Wea. Rev.*, **145**, 795–809, <https://doi.org/10.1175/MWR-D-16-0316.1>.
- Tao, D., and F. Zhang, 2014: Effect of environmental shear, sea-surface temperature, and ambient moisture on the formation and predictability of tropical cyclones: An ensemble-mean perspective. *J. Adv. Model. Earth Syst.*, **6**, 384–404, <https://doi.org/10.1002/2014MS000314>.
- , and —, 2015: Effects of vertical wind shear on the predictability of tropical cyclones: Practical versus intrinsic limit. *J. Adv. Model. Earth Syst.*, **7**, 1534–1553, <https://doi.org/10.1002/2015MS000474>.
- Torn, R. D., and C. Snyder, 2012: Uncertainty of tropical cyclone best-track information. *Wea. Forecasting*, **27**, 715–729, <https://doi.org/10.1175/WAF-D-11-00085.1>.
- Vigh, J. L., and W. H. Schubert, 2009: Rapid development of the tropical cyclone warm core. *J. Atmos. Sci.*, **66**, 3335–3350, <https://doi.org/10.1175/2009JAS3092.1>.
- Wadler, J. B., R. F. Rogers, and P. D. Reasor, 2018a: The relationship between spatial variations in the structure of convective bursts and tropical cyclone intensification as determined by airborne Doppler radar. *Mon. Wea. Rev.*, **146**, 761–780, <https://doi.org/10.1175/MWR-D-17-0213.1>.
- , J. A. Zhang, B. Jaimes, and L. K. Shay, 2018b: Downdrafts and the evolution of boundary layer thermodynamics in Hurricane Earl (2010) before and during rapid intensification. *Mon. Wea. Rev.*, **146**, 3545–3565, <https://doi.org/10.1175/MWR-D-18-0090.1>.
- , —, R. F. Rogers, B. Jaimes, and L. K. Shay, 2021: The rapid intensification of Hurricane Michael (2018): Storm structure and the relationship to environmental and air–sea interactions. *Mon. Wea. Rev.*, **149**, 245–267, <https://doi.org/10.1175/MWR-D-20-0145.1>.
- Wang, X., and H. Jiang, 2021: Contrasting behaviors between the rapidly intensifying and slowly intensifying tropical cyclones in the North Atlantic and eastern Pacific basins. *J. Climate*, **34**, 987–1003, <https://doi.org/10.1175/JCLI-D-19-0908.1>.
- Wang, Y., and C.-C. Wu, 2004: Current understanding of tropical cyclone structure and intensity changes—A review. *Meteor. Atmos. Phys.*, **87**, 257–278, <https://doi.org/10.1007/s00703-003-0055-6>.
- Zagrodnik, J. P., and H. Jiang, 2014: Rainfall, convection, and latent heating distributions in rapidly intensifying tropical cyclones. *J. Atmos. Sci.*, **71**, 2789–2809, <https://doi.org/10.1175/JAS-D-13-0314.1>.
- Zawislak, J., H. Jiang, G. R. Alvey, E. J. Zipser, R. F. Rogers, J. A. Zhang, and S. N. Stevenson, 2016: Observations of the structure and evolution of Hurricane Edouard (2014) during intensity change. Part I: Relationship between the thermodynamic structure and precipitation. *Mon. Wea. Rev.*, **144**, 3333–3354, <https://doi.org/10.1175/MWR-D-16-0018.1>.
- Zhang, F., and D. Tao, 2013: Effects of vertical wind shear on the predictability of tropical cyclones. *J. Atmos. Sci.*, **70**, 975–983, <https://doi.org/10.1175/JAS-D-12-0133.1>.